Appendix A

A Study of the Timing Properties of Position-sensitive Avalanche Photodiodes

This paper describes work done in collaboration with Simon Cherry's group at the University of California, Davis. The timing of scintillation signals emanating from different areas of the PSAPD surface were found to be related to the distance from readout pins. An algorithm was developed to normalize for this effect for PSAPD detector-based PET systems. I was involved in the setup of the experimental apparatus to characterize the PSAPD timing properties and contributed software towards the implementation of the algorithm.

A study of the timing properties of position-sensitive avalanche photodiodes

Yibao Wu[1], **Thomas SC Ng**[2], **Yongfeng Yang**[1], **Kanai Shah**[3], **Richard Farrell**[3], and **Simon R Cherry**[1]

[1]Department of Biomedical Engineering, University of California, Davis, CA 95616, USA

[2]Beckman Institute, Department of Biology, California Institute of Technology, Pasadena, CA 91125, USA

[3]Radiation Monitoring Devices, Inc. Watertown, MA, USA

Abstract

In this paper we study position-dependent timing shifts and timing resolution in position sensitive avalanche photodiodes (PSAPDs) and their effect on the coincidence window used in positron emission tomography (PET) systems using these devices. There is a delay in PSAPD signals that increases as the excitation position moves from the corner to the center of the device and the timing resolution concurrently worsens. The difference in timing between the center and corner can be up to 30.7 ns for a 14×14 mm^2 area PSAPD. This means that a PSAPD-based PET system could require a very wide coincidence timing window (>60 ns) if this effect is not corrected, although the individual crystal pairs still have full-width half-maximum (FWHM) timing resolutions better than 7.4 ns. In addition to characterizing the timing properties of PSAPDs, two correction methods were developed and applied to data from a pair of PSAPD detectors. These two timing offset corrections reduced the timing shift of a crystal pair from 52.4 ns to 9.7 ns or 1.3 ns, improved FWHM timing resolution of the detector pair from 24.6 ns to 9.5 ns or 6.0 ns and reduced the timing window (sufficient to cover at least twice the FWHM for all crystal pairs) from 65.1 ns to 22.0 ns or 15.2 ns respectively. A two-step timing alignment method is proposed for a PET system consisting of multiple PSAPDs. Lastly, the effect of PSAPD size on the timing performance was also evaluated.

Keywords

photodiodes; photodetectors; instrumentation; PET

1 Introduction

The use of position sensitive avalanche photodiodes (PSAPDs) is emerging as an interesting alternative to traditional photodetector technology such as photomultiplier tubes (PMT) for positron emission tomography (PET) detector development (Shah *et al.*, 2004; Catana *et al.*, 2006; Zhang *et al.*, 2007; Yang *et al.*, 2008). The small size of PSAPD-based detectors compared to more bulky PMT-based types may be advantageous for use in confined geometries. Compact detector designs possible with PSAPDs allow for scanner configurations with increased sensitivity and high and uniform spatial resolution. PSAPDs also have high

161

quantum efficiency, a wide spectral response and are insensitive to magnetic fields (Pichler *et al.*, 2006). Thus, PSAPD-based PET detectors have been adapted for applications such as depth-of-interaction (DOI)-encoding (Yang *et al.*, 2008) and MR-compatible PET systems (Catana *et al.*, 2008). Although one of the main advantages of using PSAPDs compared to conventional avalanche photodiodes (APDs) is the significant reduction in the number of electronic readout channels, this technology also presents challenges compared to APD- and PMT-based detectors. The most obvious, though most easily addressed, challenge is the pin-cushion distortion of spatial positional readout information due to the non-linear fashion in which charge is shared among the four corner anodes (Shah *et al.*, 2004). Several groups have proposed both software (Despres *et al.*, 2007; Zhang *et al.*, 2007; Chaudhari *et al.*, 2008) and hardware (Grazioso *et al.*, 2002; Shah *et al.*, 2002) solutions to correct or account for this distortion for flood map histogram discrimination. One other notable effect that our group has observed is the apparent time shift between signals originating from the center of the PSAPD versus those from the edges or corners. Previous studies have noted a timing shift of up to 25 ns (Catana *et al.*, 2006). This has been attributed to the resistive readout present on PSAPDs. In order to maintain the high spatial resolution offered by a crystal array setup while capturing all coincidence events, a wide timing coincidence window of 80 ns is currently used in our PSAPD-based detectors. Here, we further characterize the time difference of signals originating from different positions on the PSAPD and explore their dependence on the size of the PSAPD. Using this information, we propose an approach to correct the timing signal after signal read out from the detector to the data processing portion of the system. The ability to correct for this timing shift will improve the timing resolution of a crystal array/PSAPD-based detector and reduce sensitivity to random events via much tighter coincidence windowing.

2 Materials & Methods

2.1 Timing shift and timing resolution at various locations on PSAPD surface

To determine the timing shift and timing resolution at different locations on the surface of a PSAPD, an experimental setup was built as shown in Figure 1. A 14×14 mm^2 PSAPD was coupled to three individual LSO crystals each of size $1.43 \times 1.43 \times 6$ mm^3. The crystals were polished on all sides and wrapped with teflon tape on five sides except the one coupled to the PSAPD. The three crystals were placed at three representative locations, corner, edge and center, using a positioning guide made of teflon. Optical coupling between the LSO crystals and PSAPD was accomplished using optical grease (BC-630, Saint-Gobain Ceramics & Plastics, Inc., Newbury, OH). A PMT (R580, Hamamatsu, Hamamatsu City, Japan) coupled to a single LSO crystal with size of $1.5 \times 1.5 \times 20$ mm^3 was used as the timing reference. The separation between the front surfaces of the two detectors was 60 mm. A ^{22}Na point-like source with activity 23 µCi was placed at the center of the setup.

The signal from the PMT was buffered with a fan-out unit (740, Philips Scientific, Mahwah, NJ); one output was fed to an ORTEC 584 constant fraction discriminator (CFD) (Advanced Measurement Technology, Inc., Oak Ridge, TN) and the generated trigger was used for PMT timing. The delay for the CFD was ~3 ns. Another fan-out output was shaped with a shaping amplifier (N568B, CAEN Technologies, Staten Island, NY) and fed to a data acquisition (DAQ) board (PD2-MFS-2M/14, United Electronic Industries, Inc., Walpole, MA). The shaping time was 1 µs.

Signals from the PSAPD were first amplified with 5 CR-110 charge sensitive pre-amplifiers (Cremat, Watertown, MA). The cathode signal from the PSAPD was then shaped using a fast filter amplifier (ORTEC 579) with a differentiation and integration time of 10 ns and fed to a CFD to generate the timing signal for the PSAPD. The shaped signal from the corner was observed to have a rise time of 55 ns and fall time of 110 ns and the signal from the center had a rise time of 80 ns and fall time of 160 ns. The delay for the CFD was ~45 ns. The 4 anode

162

signals from the PSAPD were shaped using the N568B shaping amplifier with a shaping time of 1 µs and recorded by the data acquisition system.

A coincidence trigger was made from the timing signals obtained from the PMT and PSAPD using a coincidence unit (Philips Scientific 756). The trigger was then delayed and width-extended using a delay and gate generator (ORTEC 416A) before being sent to the DAQ system as the trigger. The coincidence timing window 2τ was set to 88 ns where τ was the width of the trigger signals from the PMT and PSAPD. To ensure correct timing for coincidence processing, a delay of 72 ns was introduced to the PMT timing signal before being passed to the coincidence unit to account for the intrinsic timing delay between PMT and PSAPD signals. The position-dependent timing difference between the PMT and PSAPD was measured with a time-to-analog convertor (TAC) unit (ORTEC 566). The PMT timing signal was used as the start signal and the PSAPD timing signal was used as the stop signal. The output was recorded by the DAQ system. In-house developed DAQ software was used to store the raw data (Judenhofer *et al.*, 2005).

The timing spectrum for each crystal was generated and analyzed. The centroid of the timing spectra (with respect to an arbitrary reference time) and the full-width at half-maximum (FWHM) of the timing spectra (corresponding to the timing resolution) were calculated for each crystal. The timing shift is defined as the difference in the centroid locations for events occurring in two different crystals. The CFD thresholds were set just above the noise (~60 keV) and no software energy windows were applied, either for the PMT or PSAPD signals.

2.2 Timing shift and timing resolution of a crystal array on a PSAPD

A setup similar to Figure 1 was used to measure the timing shift and timing resolution of a complete LSO crystal array on a PSAPD. The individual crystals on the PSAPD were replaced with an array consisting of 8×8 crystal elements, where the size of each element was 1.43×1.43×6 mm^3. The dimension of the whole array was 12×12×6 mm^3 thus it covered 73% of the area of the PSAPD. The array was centered on the PSAPD with a positioning guide made of teflon. The single crystal on the PMT was replaced with an LSO crystal array. The crystal array was composed of 12×12 individual crystals with size of 1.51×1.51×10 mm^3 and the size of array was 19.2×19.2×10 mm^3. An LSO array was used on the PMT because it is impractical to perform the experiment using the movable stage with a point source. The ^{22}Na source was replaced with a cylindrical ^{68}Ge source and placed at the center of setup. The cylindrical source had a diameter of 25 mm and a length of 50 mm, and its activity was 71 µCi. A cylindrical source was chosen to avoid constrained solid angles that might bias the results. The separation between the front surfaces of the two detectors was 120 mm and the source was placed at the center of the setup.

The digitized timing and energy data were acquired, and the flood histogram was generated with the energy data and segmented with a method modified from (Chaudhari *et al.*, 2008). The timing data were assigned to each crystal based on the crystal lookup table (LUT). Timing spectra were generated and the shift of the centroid of the timing spectrum and the timing resolution of each crystal measured. The spectra of the three selected locations closest to the ones described in Section 2.1 were compared to the results obtained with the individual crystals.

2.3 Timing shift and resolution between a pair of crystal array-PSAPD detectors

The experimental setup shown in Figure 2 was used to measure the timing shift and timing resolution between two PSAPD detectors. The same 8×8 LSO arrays described in Section 2.2 were centered on the PSAPDs with positioning guides made of teflon. Coincidences were determined directly from the two detector triggers. The timing window 2τ was 88 ns. A delay of 64 ns was added to the timing signal of one PSAPD, which was then used as the stop signal

163

for TAC. This PSAPD detector is denoted PSAPD1. The other PSAPD detector is used as the start signal for the TAC and is denoted PSAPD2. The separation between the front surfaces of the two detectors was 120 mm and the same ^{68}Ge source was placed at the center of setup.

To collect sufficient information for timing alignment, a cylindrical source was chosen which was large enough to cover coincidence events between all individual crystal pairs. This measurement does not require that all pairs have exactly the same number of events. If a point source had been used, the overall timing spectrum might be artificially narrow because only a few LORs are intersecting the source.

Flood histograms and crystal LUTs were generated from the data acquired. Each event was assigned to a pair of crystals based on crystal LUTs. The timing spectrum for each pair of crystals was created and the shift of the timing centroid and the FWHM timing resolution of each pair calculated. In addition, a corner crystal on PSAPD2 was chosen as a reference crystal and the shift in the timing centroid and the FWHM timing resolution of all the crystals in the PSAPD1 detector with respect to this crystal were calculated.

2.4 Timing alignment using PMT-based detector as a reference (Method 1)

To improve the timing resolution of the pair of detectors and therefore reduce the coincidence timing window required, the timing shift differences between individual crystal pairs need to be corrected by applying a calibration offset to each pair. All PET systems generate coincidence events from single events in a coincidence unit, either in hardware or software, either centralized or distributed. A direct time alignment approach can be implemented in the coincidence processing unit, during coincidence processing, where the timing shifts of all crystal pairs are aligned by applying an offset to each crystal pair. However, this approach is not practical for two reasons. Firstly, the offset lookup table required is large, on the order of N^2, where N is the total number of crystals in the whole system. Secondly, it requires complex coincidence logic; a wide coincidence window is still needed initially to find all possible coincidence events. The offset would then need to be applied from the offset LUT. Only at this point can coincidence events within a narrower coincidence window be selected. In contrast, a component-based approach can be implemented in either the coincidence or single event processing units. The difference here from the direct method is that the offset is applied to each single event using the offset value for the corresponding crystal before forming a coincidence event.

For the component-based approach, there are two ways to generate the offset LUT. One is to use a PMT-based detector as a reference, i.e. use the timing offset table derived from the timing data from a crystal array/PSAPD detector with a PMT-based detector. This would use the data generated in Section 2.2, and will be called Method 1. Method 2 uses offset tables derived from timing data obtained from a pair of PSAPD detectors, and is discussed in the next section.

For Method 1, each PSAPD can use either the same timing offset LUT (assumes timing shifts are invariant across different PSAPDs of the same size) or LUTs can be obtained for each detector separately (not studied here) in reference to a PMT-based detector. Although each individual offset LUT includes a fixed value which incorporates the intrinsic timing delay between the PMT and PSAPD signals, this cancels out if the same offset LUT is used for the two PSAPDs. A difference between the two fixed values will be included if different offset LUTs are used. However, this is not an issue for alignment correction because these timing differences only change the mean value of final timing spectra. This mean value can be subtracted. Implementation of this is further discussed in Section 4.2.

In a PET system, individual time alignment LUTs can be acquired if the detectors can be removed for individual measurement or the system has spare readout channels to insert a timing

164

probe (Moses and Thompson, 2006) to determine multiple LUTs simultaneously. Here, we compare the use of a single, common offset LUT applied to both PSAPD detectors (Method 1) versus the use of a unique LUT for each detector (Method 2). The hypothesis is that if the timing differences are dominated by effects intrinsic to the PSAPD design, then a single common offset LUT may be sufficient for accurate time alignment. In this case, the two methods should give similar improvements in timing resolution. All offset tables were applied with a step-size of 0.3125 ns to mimic the resolution of typical commercial PET electronic systems (Musrock *et al.*, 2003).

The timing spectra after offset correction were calculated and compared with the results obtained before correction. A coincidence timing window was calculated that would be sufficient to cover at least twice the FWHM for all crystal pairs. To calculate the overall timing window, the left ($TW_{left,i,j}$) and right ($TW_{right,i,j}$) boundaries of the individual timing window were first calculated for each crystal pair using Equations 1 and 2, where $TS_{i,j}$ is the timing shift between crystal i from PSAPD1 and crystal j from PSAPD2 forming this pair and $FWHM_{i,j}$ is the timing resolution. The overall timing window width $TWW_{overall}$ was then calculated with Equation 3. For calculating the overall timing window after correction with Method 1, the timing shift $TS_{i,j}$ was replaced by the timing shift after correction $TS_{i,j} - (TS_{i,PMT} - TS_{j,PMT})$.

$$TW_{left,i,j} = TS_{i,j} - FWHM_{i,j} \tag{1}$$

$$TW_{right,i,j} = TS_{i,j} + FWHM_{i,j} \tag{2}$$

$$TWW_{overall} = \max_{i,j}(TW_{right,i,j}) - \min_{i,j}(TW_{left,i,j}) \tag{3}$$

2.5 Timing alignment using a pair of PSAPD-detectors (Method 2)

Method 2 generates two different LUTs, one for each PSAPD-detector in a pair. This may help improve the resultant timing spectra because the relative location of the crystal array coupled to the PSAPD can be slightly different for every detector and the arrays may also have slightly different characteristics, not to mention the potential timing delay differences between each PSAPD in the system. Moreover, Method 2 can be implemented without the need to remove the detectors from a system and without the use of additional electronics channels to attach external probes.

Two timing offset LUTs were generated from the data obtained with a pair of LSO array-PSAPD detectors. M_{TS}, the mean value of the timing shifts was first calculated using Equation 4 where $TS_{i,j}$ is the timing shift between crystal i from PSAPD1 and crystal j from PSAPD2 and N is the total number of crystal elements in one detector (here it was 64). The timing offset values for each crystal i from PSAPD1 ($TO_{1,i}$) and crystal j from PSAPD2 ($TO_{2,j}$) were calculated with Equations 5 and 6. To compare with the results obtained with Method 1, the offset LUTs were manually shifted to have the same mean value $M_{TS,PMT}$ as Method 1 calculated using Equation 7. As per Method 1, these timing offset LUTs include an arbitrary fixed mean value $M_{TS,PMT}$, but this can be subtracted. For each pair, the offset $TOP_{i,j}$ was calculated using Equation 8 and applied to the timing data.

165

$$M_{\text{TS}} = \sum_{i,j} \text{TS}_{i,j}/N^2 \tag{4}$$

$$\text{TO}_{1,i} = M_{\text{TS,PMT}} + \sum_{j}(\text{TS}_{i,j} - M_{\text{TS}})/N \tag{5}$$

$$\text{TO}_{2,j} = M_{\text{TS,PMT}} - \sum_{i}(\text{TS}_{i,j} - M_{\text{TS}})/N \tag{6}$$

$$M_{\text{TS,PMT}} = \sum_{i} \text{TS}_{i,\text{PMT}}/N \tag{7}$$

$$\text{TOP}_{i,j} = \text{TO}_{1,i} - \text{TO}_{2,j} \tag{8}$$

The timing shifts and coincidence timing window (same definition as in Section 2.4) after timing alignment correction were calculated and compared with those obtained with no timing alignment in Section 2.3. For calculating the overall timing window after correction with Method 2, the timing shift $TS_{i,j}$ was replaced by the timing shift after correction $TS_{i,j} - TOP_{i,j}$.

2.6 PSAPD size effect on timing

With larger area PSAPDs, more detector elements can be decoded with one photodetector and less electronics channels are needed per unit detector area. Due to the finite deadspace of the packaging around PSAPDs, this also increases the packing fraction, potentially increasing the sensitivity that is of significance for PET applications. However, the timing shift is mainly caused by the capacitance of the PSAPD and the resistive readout on the anode side that provides spatial location information. Increasing the size of the PSAPD should increase the capacitance and cause greater timing shifts between different regions of the PSAPD. To explore this, we compared the timing shifts measured from a 20×20 mm^2 PSAPD to those from a 14×14 mm^2 PSAPD, using the methods described in Section 2.1. The signal from a corner crystal had similar rise time and fall time to those observed with the 14×14 mm^2 PSAPD. As the signal from the center of a 20×20 mm^2 PSAPD was very slow (rise time of ~150ns and fall time of ~300ns), the timing shift was studied at two different CFD delays of 45 and 125 ns.

3 Results

3.1 Timing shift and timing resolution at various locations on PSAPD surface

Figure 3 shows the timing spectra at three representative locations on a PSAPD. The timing is measured relative to the PMT signal, so each centroid includes a fixed value corresponding to the timing delay between the PMT and PSAPD. The corner position had the fastest signal and the best timing resolution of 2.3 ns while the center position had the slowest signal and worst timing resolution of 3.9 ns. The timing shift between the corner and the center crystals was 30.7 ns. Because of this shift, current PET systems using PSAPD technology need a wide timing window to accept coincident events from all locations across the surface of the PSAPDs.

166
This necessarily increases the random events detected as well, decreasing the noise equivalent count rate (NECR), especially at high count rates.

3.2 Timing shift and timing resolution of a crystal array on a PSAPD

The timing characteristics for each crystal of an LSO array/PSAPD detector in coincidence with a PMT-based detector are plotted as a spatial distribution map in Figures 4a and 4b. The timing centroids had a standard deviation of 6.8 ns and the maximum timing shift was 26.9 ns. For timing resolutions, mean values of 3.4 ns with a standard deviation of 0.3 ns were observed with a maximum value of 3.9 ns and a minimum of 2.5 ns. The timing spectra for three crystal locations, corner, edge and close to the center are shown in Figure 4c. In agreement with the single crystal data, the results showed that corner locations had the fastest signal and best timing resolution of 2.8 ns and the central locations had slower signals and a worse timing resolution of 3.5 ns. The timing shift from the corner to center was 23.6 ns. The reduction in timing shift compared with the single crystal data of Section 3.1 is presumably due to some light sharing between crystals, which results in a greater spread of the scintillation light once it reaches the PSAPD surface.

3.3 Timing shift and resolution between a pair of crystal array-PSAPD detectors

The map of the centroids of the timing spectra is shown for each pair of crystals in Figure 5a and the histogram of these centroid locations is shown in Figure 5b. The 64 crystals in the array in Figure 5a are numbered horizontally with 1 corresponding to the top left corner, 8 to the top right corner and 64 to the bottom right corner of the array. The timing centroids had a standard deviation of 9.5 ns and the maximum timing shift was 52.4 ns. The timing resolution map and the corresponding timing resolution histogram for each pair of crystals are shown in Figures 5c and 5d respectively. A mean FWHM timing resolution of 5.2 ns with a standard deviation of 0.6 ns was measured, with a maximum value of 7.4 ns of and a minimum value of 3.0 ns.

The centroid of the timing spectra and the timing resolutions for the crystals in PSAPD1 in coincidence with one corner crystal of PSAPD2 (opposing to the corner crystal on PSAPD1) are plotted in Figures 6a and 6b. Three representative locations were chosen and the timing spectra are plotted in Figure 6c. The results showed that the corner crystal had the fastest signal and timing resolution of 4.0 ns while the center had the slowest signal and worst timing resolution of 5.3 ns. The timing shift difference from the corner to the center was 23.8 ns.

3.4 Timing alignment using PMT-based detector as a reference (Method 1)

The timing offset LUT derived from Section 3.2 was applied to both PSAPDs. A map of the timing centroid for all crystal pairs after offset correction is plotted in Figure 7a (same scale as Figure 5a) and in Figure 7b (expanded scale). The histogram of the timing centroids is plotted in Figure 7c. The timing centroids had a standard deviation of 2.3 ns and the maximum timing shift was 9.7 ns. The measured averaged timing spectra of the pair of arrays before correction (red line) and after correction using Method 1 (green line) are plotted in Figure 10. The FWHM timing resolutions of the pair of arrays were 24.6 and 9.5 ns before and after correction respectively. The required timing window improved from 65.1 ns to 22.0 ns after correction.

From Figures 7a and 7b, it is apparent that using the same offset LUT to correct both PSAPDs does not align all crystal pairs evenly. The maximum residual timing shift of 9.7 ns is still greater than the worst FWHM timing resolution of 7.4 ns measured between crystal pairs, thus these residual timing shifts still are the primary determinant of the timing window. This suggests that using one LUT is not likely the optimal method for time alignment.

167

3.5 Timing alignment using a pair of PSAPD-detectors (Method 2)

The timing offset LUTs generated from the two individual PSAPDs are shown in Figure 8. PSAPD1 which was used in the LSO array-PSAPD versus PMT measurements had almost the same offset table as measured previously (Figure 4a) while PSAPD2 had slightly different behavior (difference up to 4.5 ns), although overall metrics were similar. The timing offset table of PSAPD1 had a mean value of 89.7 ns, standard deviation of 6.8 ns, a maximum value of 100.6 ns and a minimum value of 73.8 ns. The timing offset table of PASPD2 had a mean value of 89.7 ns, standard deviation of 6.7 ns, maximum of 100.3 ns and minimum of 74.8 ns.

A map of the timing centroids for all crystal pairs after correction is shown in Figure 9a (same scale as Figure 5a) and in Figure 9b with expanded scale. The histogram of these centroids is plotted in Figure 9c. The timing centroids had a standard deviation of 0.2 ns and the maximum timing shift was reduced to just 1.3 ns. Compared to the results in Figure 7, no obvious correction bias to any particular crystal pair was observed in the map. A narrower timing centroid distribution was also seen. The measured averaged timing spectrum of the pair of arrays after this timing correction was applied is plotted in Figure 10 (blue line) and the FWHM timing resolution was measured to be 6.0 ns. The timing window necessary to cover twice the FWHM timing resolution for all crystal pairs was 15.2 ns.

The results without correction and with the two time alignment correction methods are summarized in Table 1. The timing resolutions of individual crystal pairs were the same with and without correction. The difference between the maximum and minimum of the timing centroids after correction was significantly reduced from 52.4 ns to 9.7 ns or 1.3 ns respectively, and the FWHM timing resolution was improved from 24.6 ns to 9.5 ns or 6.0 ns respectively. The timing windows that could be applied were reduced from 65.1 ns to 22.0 ns or 15.2 ns respectively. The correction with one offset table for each PSAPD (Method 2) gave better results than one offset table for all PSAPDs (Method 1).

3.6 PSAPD size effect on timing

Using a 45 ns CFD delay, the results from a larger 20×20 mm^2 PSAPD are plotted in Figure 11a. The center and edge crystals had very broad and asymmetric timing spectra with a FWHM of up to 13.9 ns. The left bump observed in the timing spectra of the center crystal in Figure 11a is probably caused by triggering on noise and the right bump is likely due to energy-dependent walk when the CFD operates as a leading-edge discriminator for low energy events. With a 125 ns CFD delay (Figure 11b), all three crystals had narrow timing spectral peaks and had timing centroids of 145.4, 196.5 and 224.7 ns and FWHM of 3.3, 9.0 and 10.7 ns respectively. Compared to the 14×14 mm^2 PSAPD, the 20×20 mm^2 PSAPD had a similar timing shift effect but the magnitude of both the offset of the centroids and the FWHM were greater. These results suggest that a 45 ns CFD delay was not enough to resolve signals arising from the crystal at the center of the 20×20 mm^2 PSAPD. This signal required a longer CFD delay for proper peak resolution.

4 Discussion

4.1 Comparison of timing shift and timing resolution in different experimental setups

Moving from individual crystals (Figure 3) to crystal arrays (Figure 4c), the timing shift was reduced, from 30.7 ns to 23.6 ns, and the timing resolution degraded slightly for a crystal located at the corner (from 2.3 ns to 2.8 ns), while there was a small improvement in timing resolution for crystals located on the edge or at the center (from 3.7 ns to 3.5 ns and 3.9 ns to 3.5 ns respectively). This is presumably due to effects of light sharing within the crystal array that results in a greater spread of the scintillation light once it reaches the PSAPD surface. The exact positioning of the crystal with respect to the PSAPD surface may also contribute to the

168

small differences in timing resolution. Comparing the timing resolution obtained using a PMT reference (Figure 4c) to that obtained using one corner crystal on PSAPD2 as a reference (Figure 6c), the timing resolution became worse due to the lower timing resolution of the reference crystal (2~3 ns) and possible scattering (causing event mispositioning) in the crystal array on PSAPD1. The timing shift however remained almost the same, 23.6 ns and 23.8 ns respectively.

4.2 Implementation of timing alignment in an intact detector system

Timing alignment methods have been reported by several groups to improve timing resolution in detectors (Lenox *et al.*, 2007) or systems (Lenox *et al.*, 2006; Moses and Thompson, 2006). Because of the large timing shift in the PSAPD and potential integration with a MR system, these methods cannot be directly implemented in a PSAPD-based system. The timing correction/alignment described in Method 2 can however be implemented in a system with multiple PSAPDs in two steps: the first step is to determine the offset LUT for each PSAPD detector; this is followed by an alignment between the LUTs for all the detectors in the ring. The first step is shown in Figure 12a and can be performed in sequential pairs. In the single-ring configuration shown, there are 16 PSAPDs that are divided into 8 directly opposing pairs. The method described in Section 2.5 can be applied to each pair of PSAPDs. The mean value of each LUT can be subtracted to generate individual offset tables.

The second step is to time align the offset LUTs between all the detectors in the ring. As shown in Figure 12b, this can be achieved by choosing one PSAPD detector as the reference. In the figure, PSAPD #1 is selected as the reference and the residual offset of PSAPD #2 compared to PSAPD #1 can be calculated by acquiring coincidences between detectors 1 and 2 after applying their individual offset tables. The offset of PSAPD #3 can be obtained by using #2 as reference, and so on. The source should be placed at the center as precisely as possible to minimize measurement error. After all 16 offsets are obtained, the mean value of these 16 offsets can be subtracted to generate a unique residual offset value for each PSAPD in the ring. By adding this residual offset value of PSAPD to the offset table of each PSAPD, the final offset table for the system calibration can be achieved. The second step can be easily extended to apply to multiple-ring systems.

4.3 PSAPD size effect

Using a long CFD delay (125 ns) gave reasonable timing resolution across the surface of 20×20 mm^2 PSAPD, but it also caused energy thresholding problems, as shown in Figure 13a and 13b. For a CFD delay of 45 ns, the effective energy threshold for the corner was slightly higher than the edge and center, albeit still sufficient for adequate thresholding for a PET system. For a delay of 125 ns however, the effective threshold for the corner is much higher than the center despite having similar photopeak energies. The reason is that the constant fraction (CF) signal comes later than the duration of the thresholded signal for low energy events and therefore it is not triggered. This non-uniform response across the surface of PSAPD may cause normalization and/or random subtraction problems. The higher effective threshold associated with the longer CFD delay forces the PSAPD to work at very low threshold level, increasing the count rate and false triggers which have effects on dead time. Thus using larger PSAPDs, there is a challenge in simultaneously obtaining good energy and timing resolution because it is hard to find a CFD delay that is good for both measures. The proper functioning of a CFD relies on pulses varying only in amplitude, not in shape. But this is not the case in PSAPDs. A short delay did not provide good timing resolution because of the high noise associated with the signal. We are therefore exploring other techniques, including non-cable delay CFD (Binkley *et al.*, 2002) and other signal processing techniques, for these large-area PSAPDs.

169
Another effect that can be seen from Figure 13 is the shift of photopeak and this is due to the sampling in the DAQ. The DAQ digitizes only one peak value for each signal per event and the sampling position is determined by the DAQ trigger which is a delayed version of the coincidence trigger. A shift in the trigger location caused the shift in energy photopeak, however this is not an issue as each individual crystal is calibrated using its own photopeak. In Figure 13a, the relatively small fraction of events that exhibit energy-dependent walk and the relatively small magnitude (up to 30 ns) of that walk does not have a significant effect on energy spectra in our studies because of the long shaping time used (1 µs).

5 Conclusions & Future Work

The position-dependent timing shift and timing resolution of PSAPDs were studied and two methods to correct these phenomena were described. Moving from the corner to the center of a PSAPD, the rise time of the signal becomes slower and the timing resolution worsened. Larger area PSAPDs magnified this effect. Correction of this effect using one offset lookup table derived from events acquired between an LSO array/PSAPD detector and a PMT reduced the timing shift and improved the timing resolution, thus allowing the coincidence timing window to be tightened. Using individual offset tables derived for each individual PSAPD the shift was further reduced. This additional improvement was probably because of the other contributions to the timing shift in addition to the intrinsic effect of PSAPD design, such as positioning of crystal array or unique characteristics of each crystal array. The timing correction methods described in this study can be applied to whole detector systems with multiple PSAPDs using a two-step algorithm. Future studies will involve applying these correction methods in novel PSAPDs detector systems. Further work is needed to determine the optimal detection electronics for larger area PSAPDs where the changes in signal shape across the face of the PSAPD make it hard to simultaneously achieve good timing and energy resolution.

Acknowledgments

References

Binkley DM, Puckett BS, Swann BK, Rochelle JM, Musrock MS, Casey ME. A 10-Mc/s, 0.5-mu m CMOS constant-fraction discriminator having built-in pulse tail cancellation. IEEE Transactions on Nuclear Science 2002;49:1130–1140.

Catana C, Procissi D, Wu Y, Judenhofer MS, Qi J, Pichler BJ, Jacobs RE, Cherry SR. Simultaneous in vivo positron emission tomography and magnetic resonance imaging. Proc Natl Acad Sci U S A 2008;105:3705–3710. [PubMed: 18319342]

Catana C, Wu YB, Judenhofer MS, Qi JY, Pichler BJ, Cherry SR. Simultaneous acquisition of multislice PET and MR images: Initial results with a MR-compatible PET scanner. Journal of Nuclear Medicine 2006;47:1968–1976. [PubMed: 17138739]

Chaudhari AJ, Joshi AA, Bowen SL, Leahy RM, Cherry SR, Badawi RD. Crystal identification in positron emission tomography using nonrigid registration to a Fourier-based template. Physics in Medicine and Biology 2008;53:5011–5027. [PubMed: 18723924]

Despres P, Barber WC, Funk T, McClish M, Shah KS, Hasegawa BH. Modeling and correction of spatial distortion in position-sensitive avalanche photodiodes. IEEE Transactions on Nuclear Science 2007;54:23–29.

Grazioso, R.; Farrell, R.; Shah, KS.; Glodo, J.; Olschner, F. A novel, distortion-free position sensitive APD for nuclear imaging; Nuclear Science Symposium Conference Record, 2002 IEEE; 2002. p. 464-467.

170

Judenhofer MS, Pichler BJ, Cherry SR. Evaluation of high performance data acquisition boards for simultaneous sampling of fast signals from PET detectors. Physics in Medicine and Biology 2005;50:29–44. [PubMed: 15715420]

Lenox, M.; McFarland, A.; Burbar, Z.; Hayden, C. Coincidence timing analysis of APD based PET detectors; Nuclear Science Symposium Conference Record, 2007. NSS '07. IEEE; 2007; p. 3766-3769.

Lenox, MW.; Atkins, BE.; Pressley, DR.; McFarland, A.; Newport, DF.; Siegel, SB. Digital Time Alignment of High Resolution PET Inveon Block Detectors; Nuclear Science Symposium Conference Record, 2006. IEEE; 2006. p. 2450-2453.

Moses WW, Thompson CJ. Timing Calibration in PET Using a Time Alignment Probe. IEEE Transactions on Nuclear Science 2006;53:2660–2665.

Musrock MS, Young JW, Moyers JC, Breeding JE, Casey ME, Rochelle JA, Binkley DM, Swann BK. Performance characteristics of a new generation of processing circuits for PET applications. IEEE Transactions on Nuclear Science 2003;50:974–978.

Pichler BJ, Judenhofer MS, Catana C, Walton JH, Kneilling M, Nutt RE, Siegel SB, Claussen CD, Cherry SR. Performance test of an LSO-APD detector in a 7-T MRI scanner for simultaneous PET/MRI. Journal of Nuclear Medicine 2006;47:639–647. [PubMed: 16595498]

Shah KS, Farrell R, Grazioso R, Harmon ES, Karplus E. Position-sensitive avalanche photodiodes for gamma-ray imaging. IEEE Transactions on Nuclear Science 2002;49:1687–1692.

Shah KS, Grazioso R, Farrell R, Glodo J, McClish M, Entine G, Dokhale P, Cherry SR. Position sensitive APDs for small animal PET imaging. IEEE Transactions on Nuclear Science 2004;51:91–95.

Yang YF, Wu YB, Qi JY, James SS, Du HN, Dokhale PA, Shah KS, Farrell R, Cherry SR. A prototype PET scanner with DOI-encoding detectors. Journal of Nuclear Medicine 2008;49:1132–1140. [PubMed: 18552140]

Zhang J, Foudray AMK, Cott PD, Farrell R, Shah K, Levin CS. Performance characterization of a novel thin position-sensitive avalanche photodiode for 1 mm resolution positron emission tomography. IEEE Transactions on Nuclear Science 2007;54:415–421.
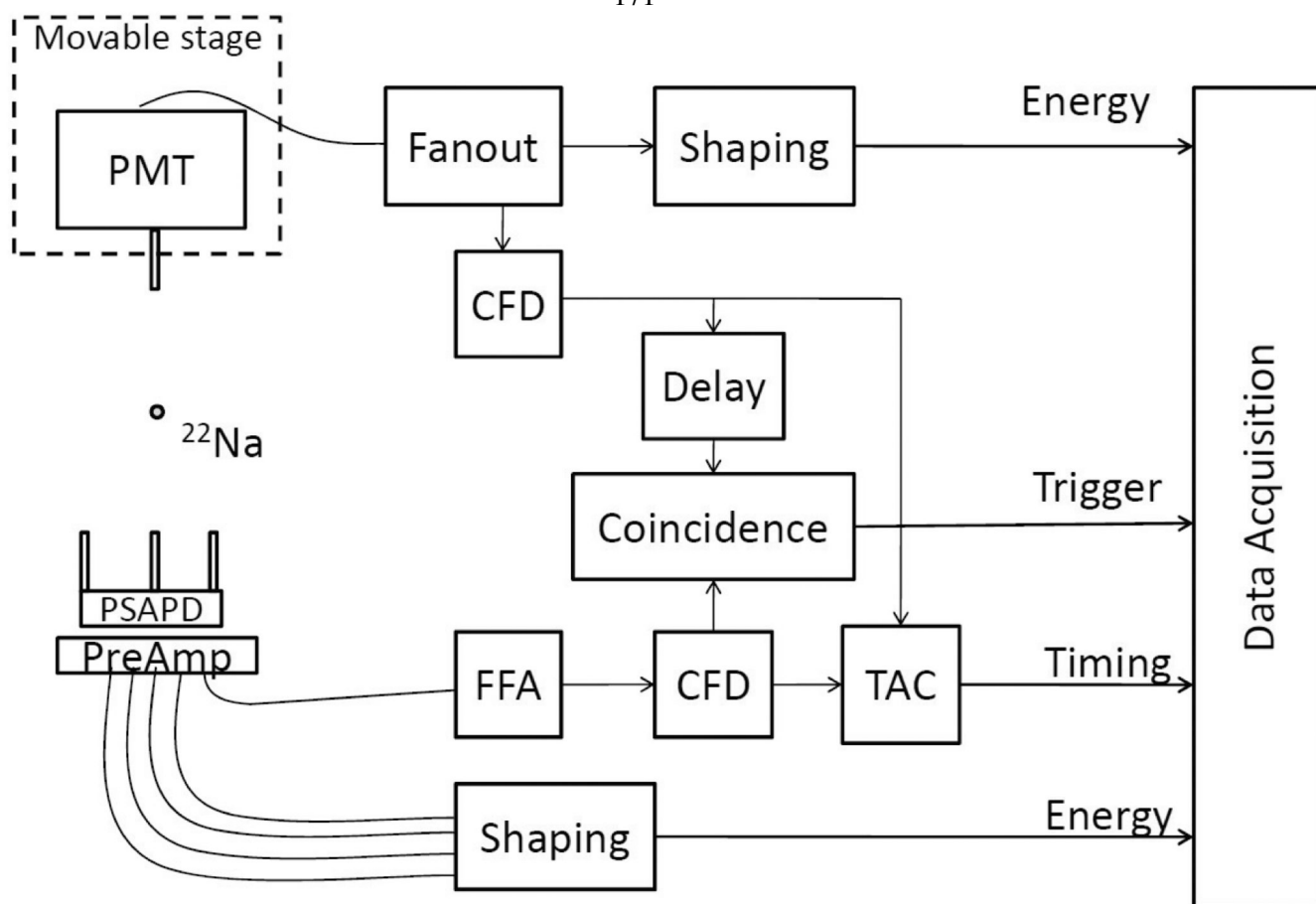
171

Figure 1.
Experimental setup for timing measurements of a PSAPD-based LSO detector in coincidence with a PMT-based LSO detector.
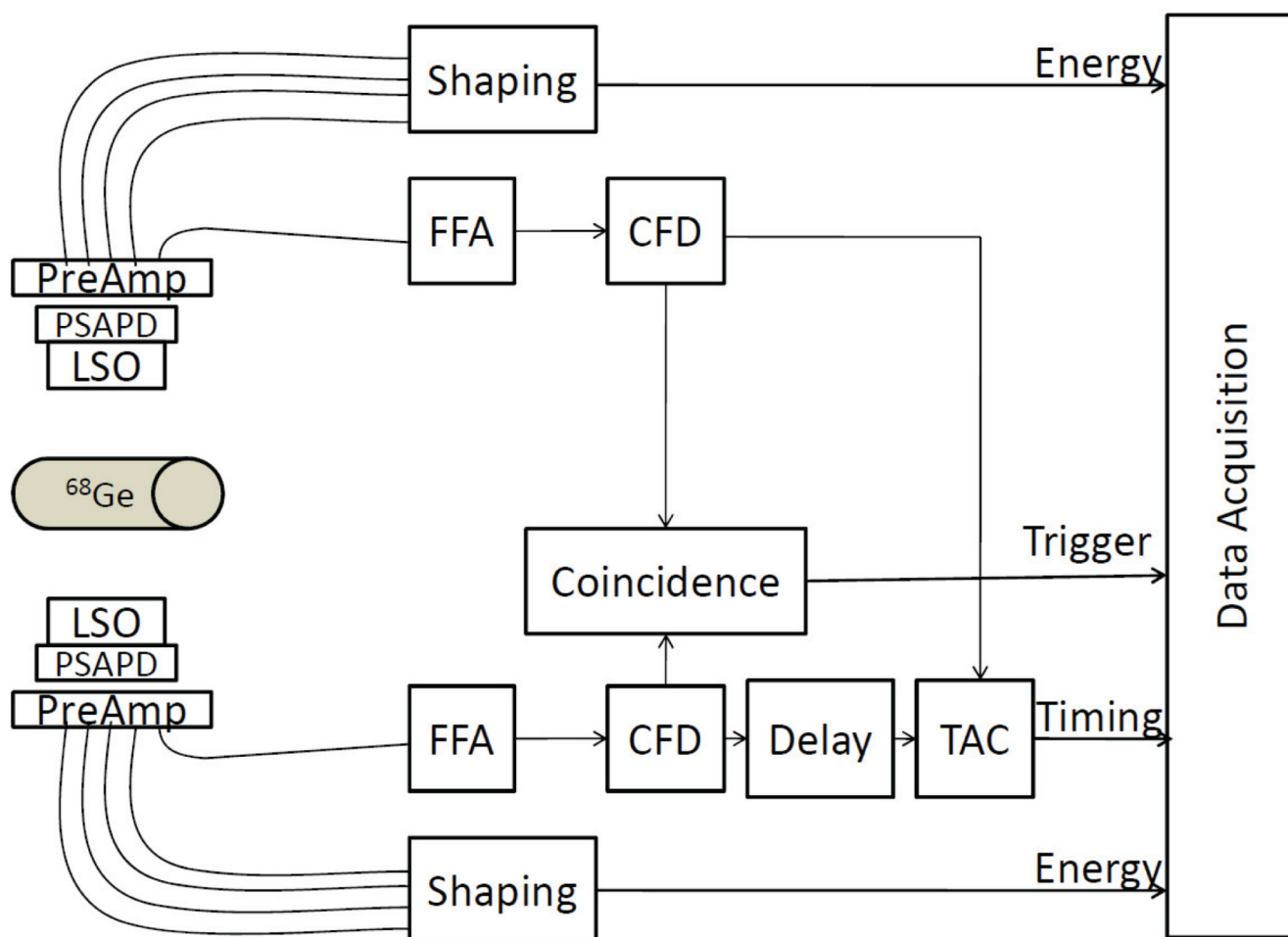
172

Figure 2.
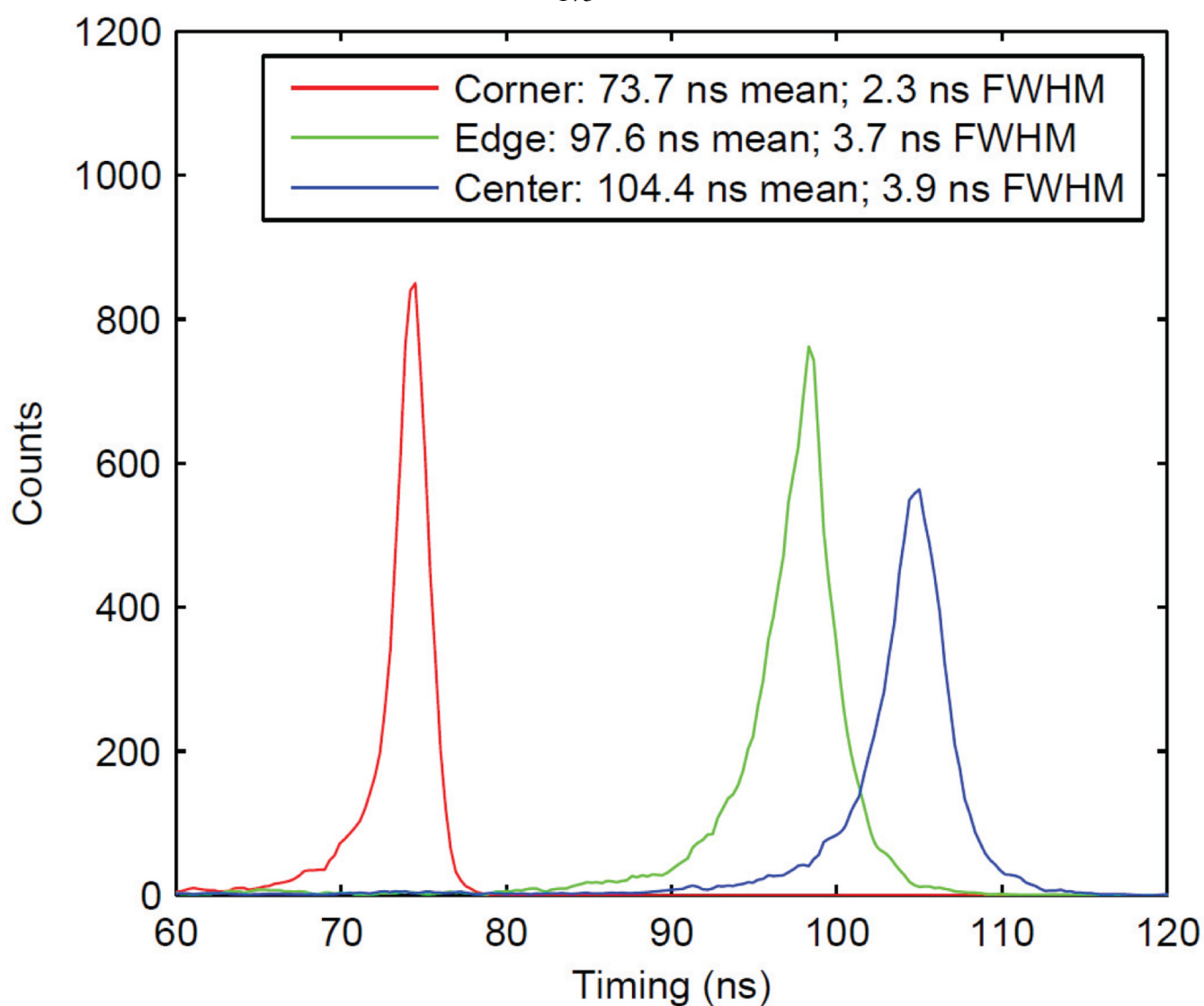Experimental setup for timing measurements of two PSAPD-based LSO detectors in coincidence.

173

Figure 3.
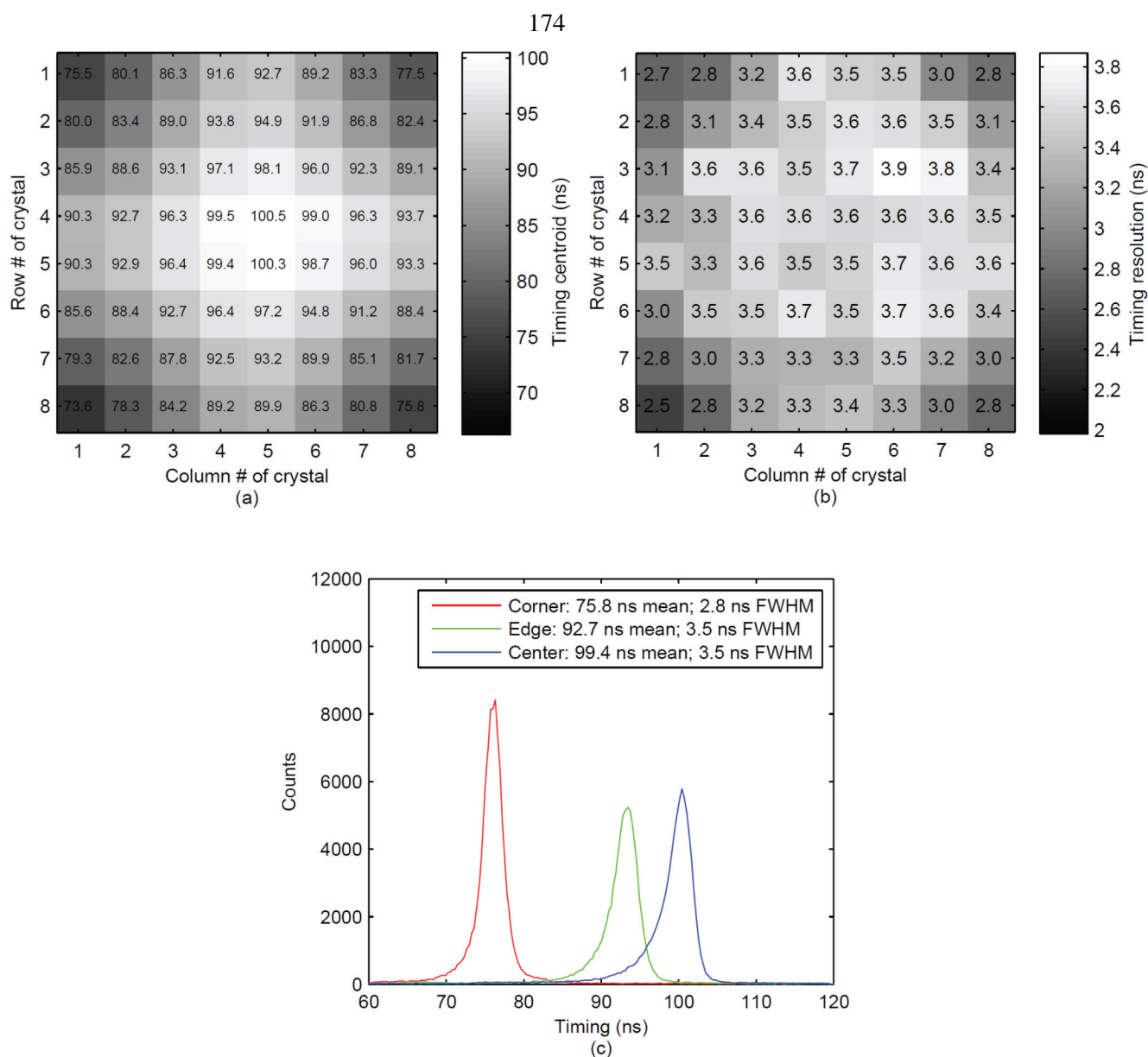Timing shift and resolution at three locations on the surface of a PSAPD.

174

Figure 4.
Spatial map of (a) the centroids of timing spectra (ns) and (b) the timing resolution (ns) for the whole array and timing spectra (c) for crystals at three representative locations on the PSAPD (comparable to the locations in Figure 3).

175
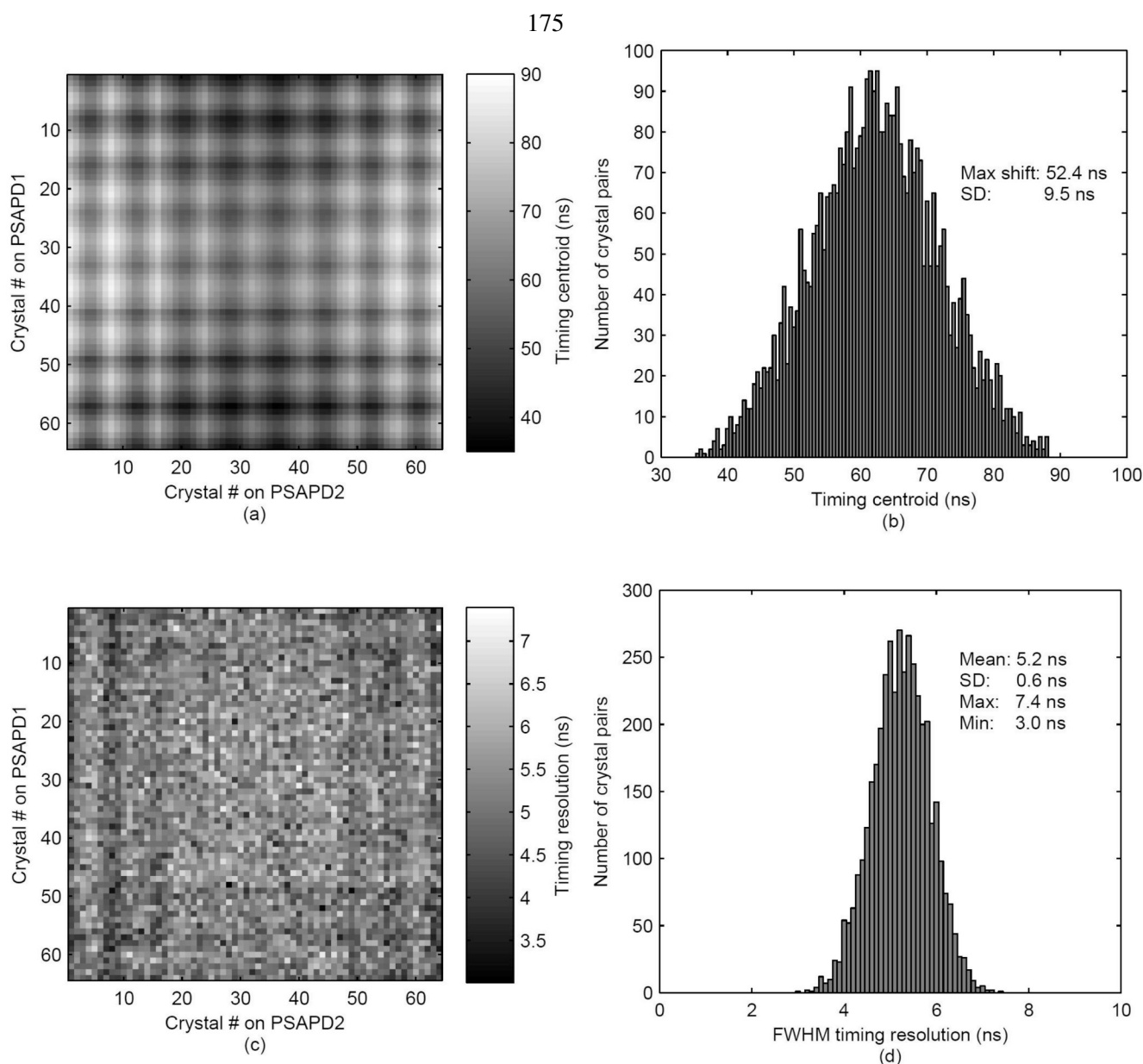
Figure 5.
Crystal-crystal map of (a) centroids of timing spectra, (b) histogram of centroids, (c) map of timing resolution and (d) histogram of timing resolution for all crystal pairs.

176
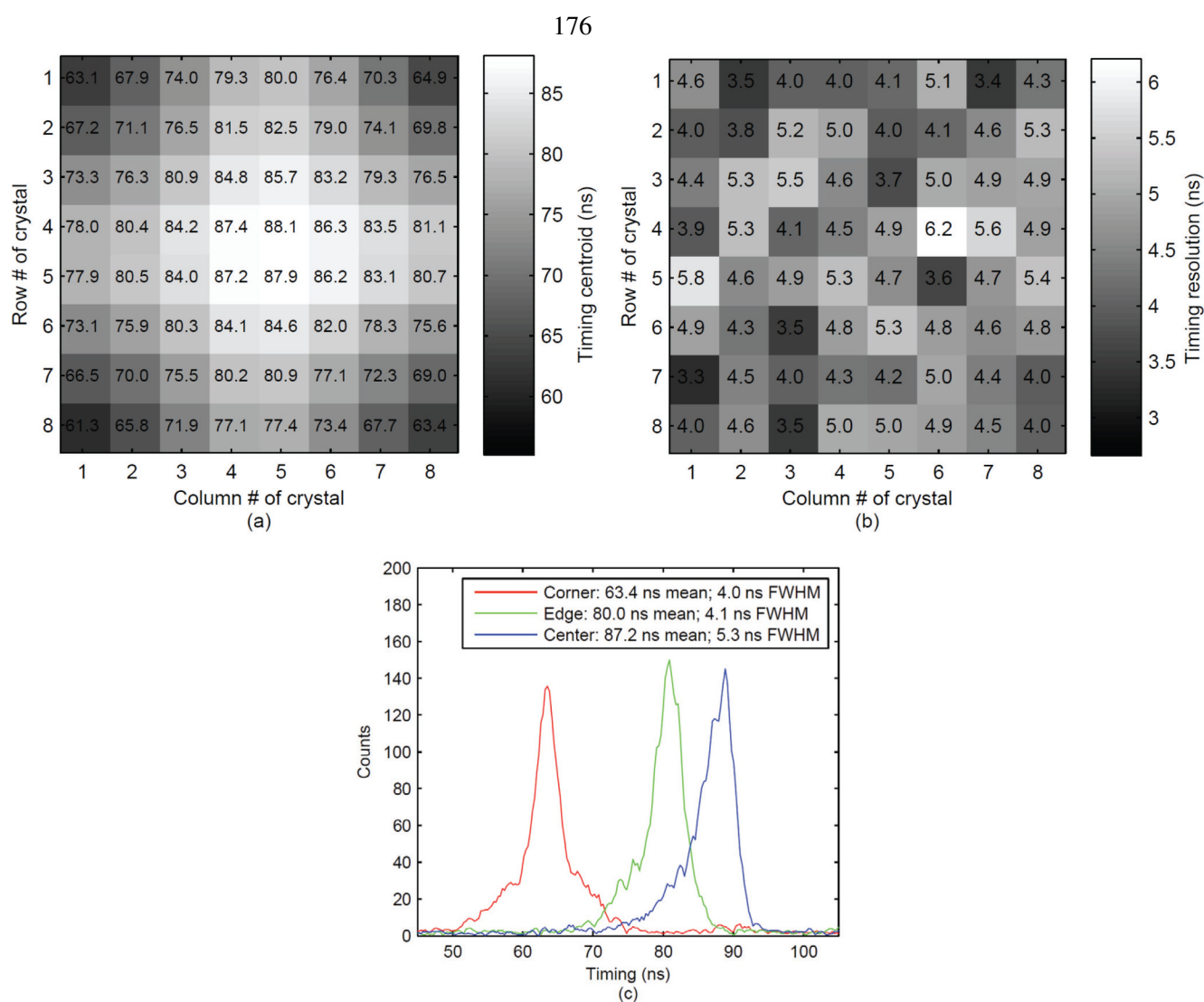
Figure 6.
Spatial map of (a) centroids of timing spectra (ns), (b) timing resolution (ns) of crystals in PSAPD1 with respect to corner crystal in PSAPD2 and (c) timing spectra for three representative locations.
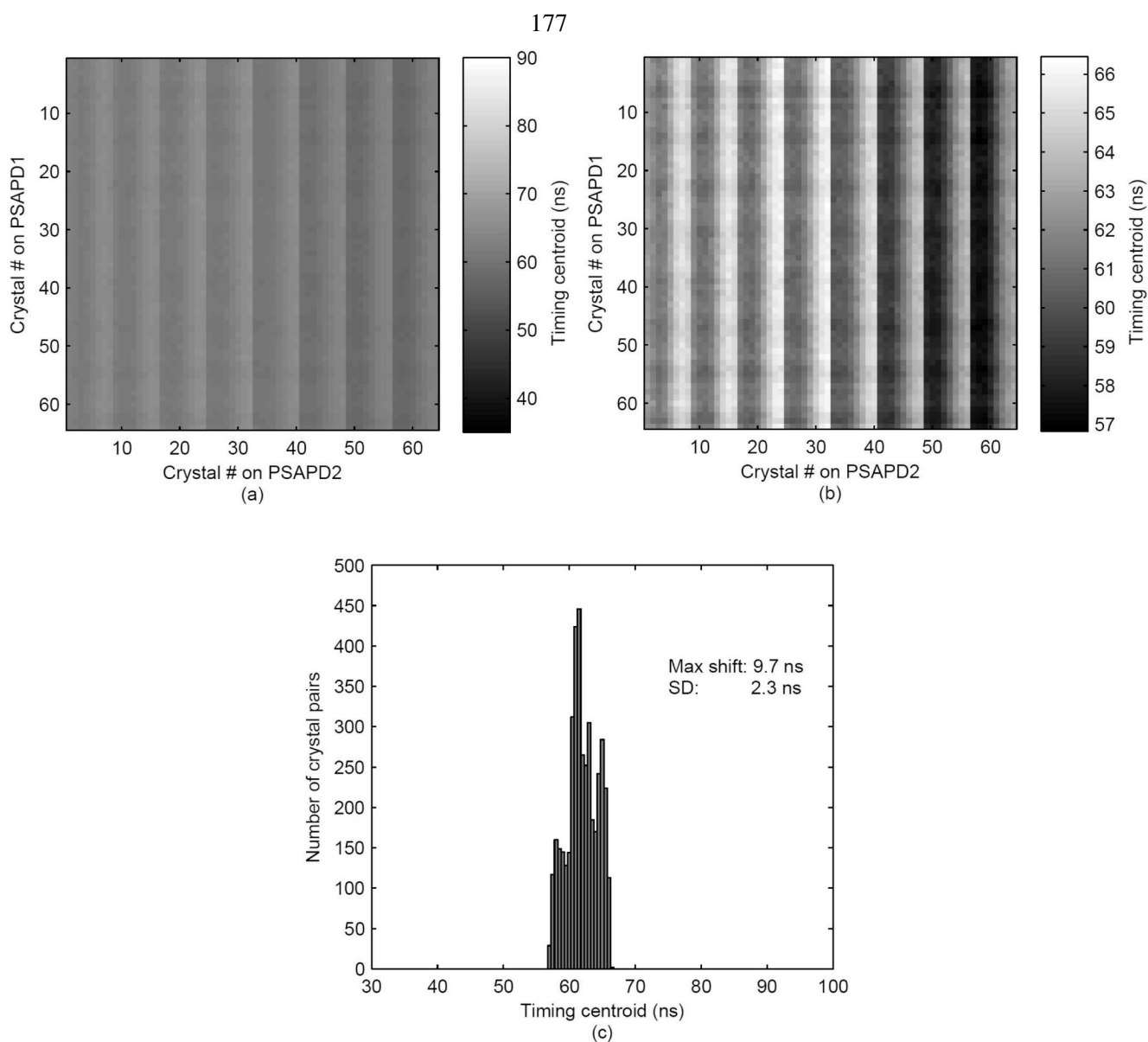
177

Figure 7.
Crystal-crystal map of timing centroids plotted (a) on same scale as Figure 5a and (b) on expanded scale, and (c) histogram of timing centroids after time alignment correction with Method 1.
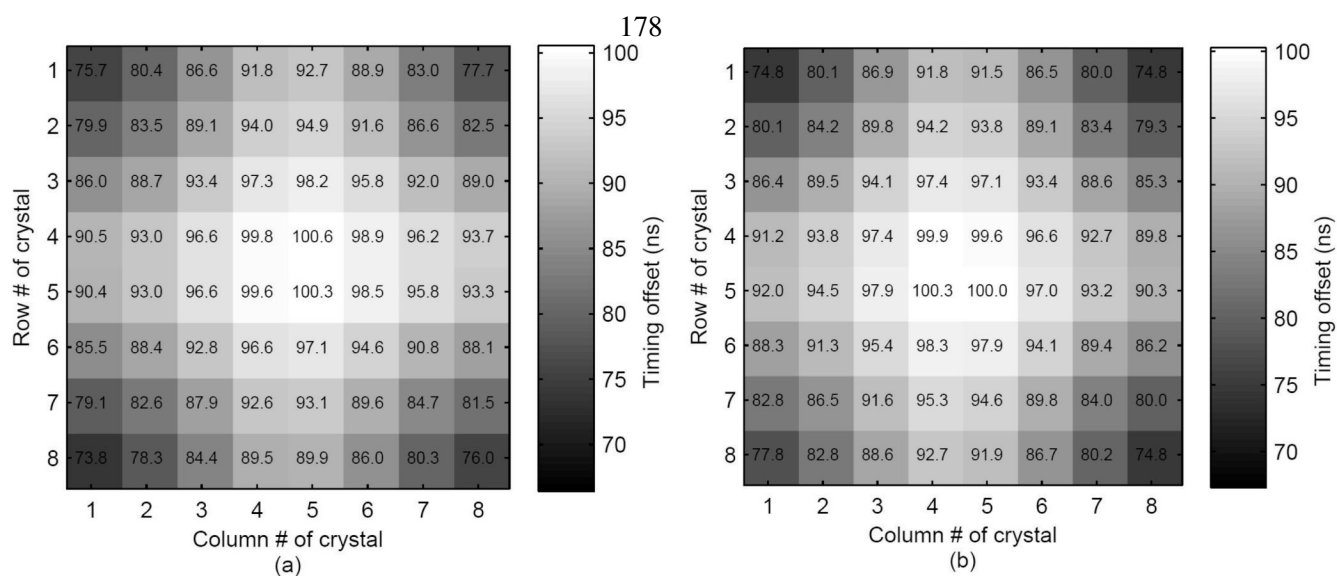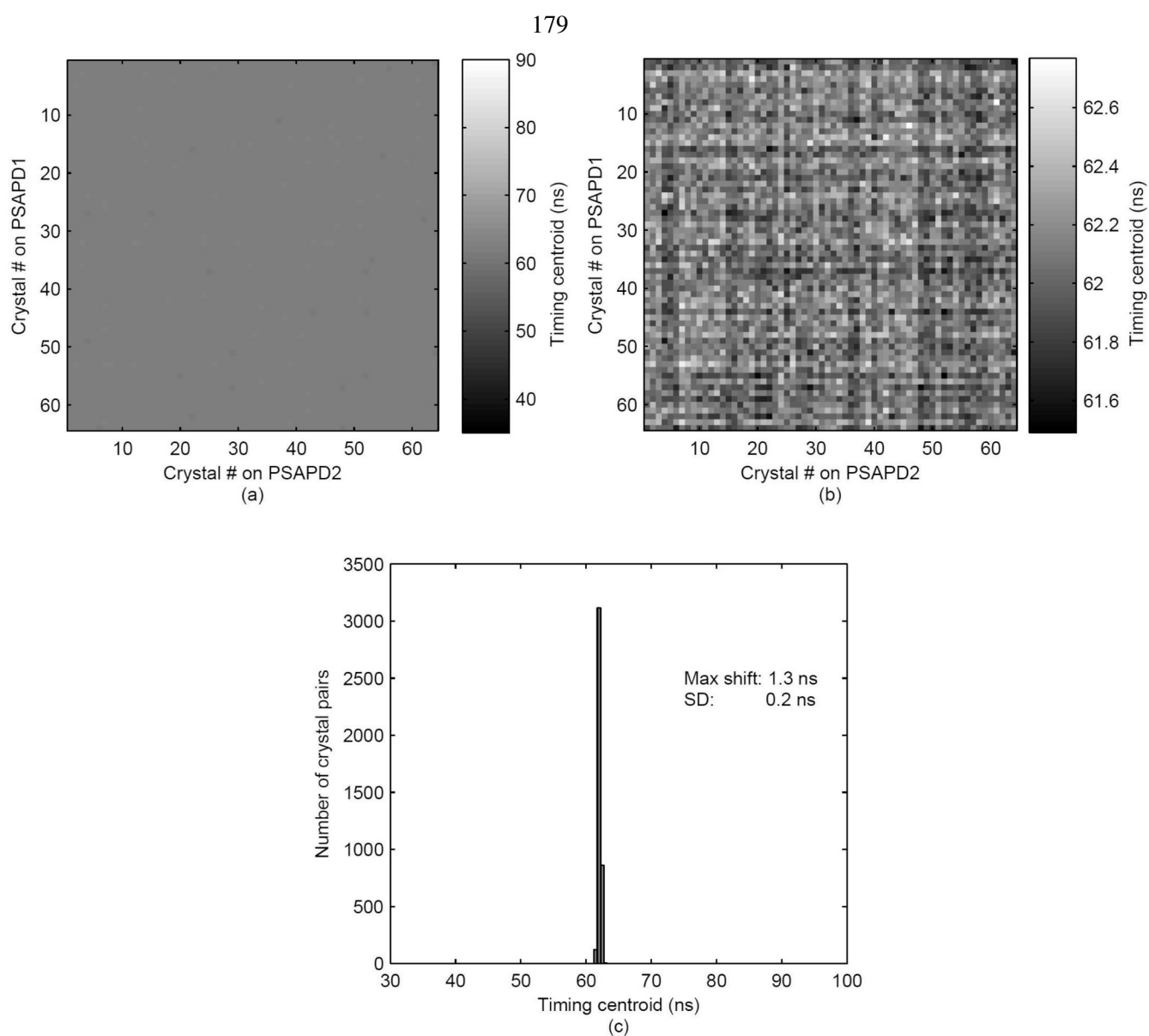
178

Figure 8.
Timing offset LUTs of (a) PSAPD1 and (b) PSAPD2 used for correction Method 2.

179

Figure 9.
Crystal-crystal map of timing centroids plotted (a) on same scale as Figure 5a and (b) on expanded scale, and (c) histogram of timing centroids after time alignment correction with Method 2.
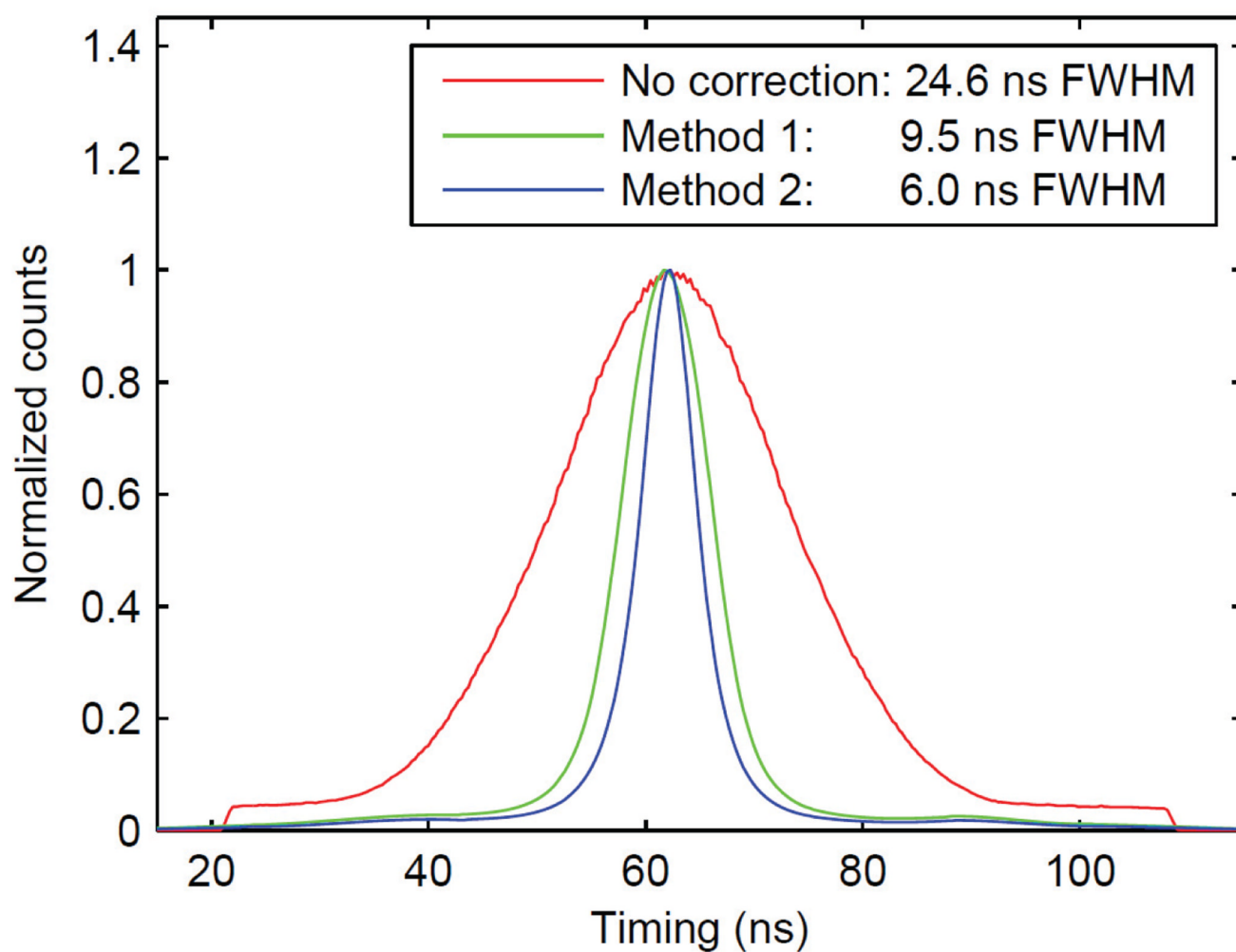
180

Figure 10.
Measured averaged timing spectra (over all crystal pairs) without (red line) and with timing offset correction Method 1 (green line) and Method 2 (blue line).
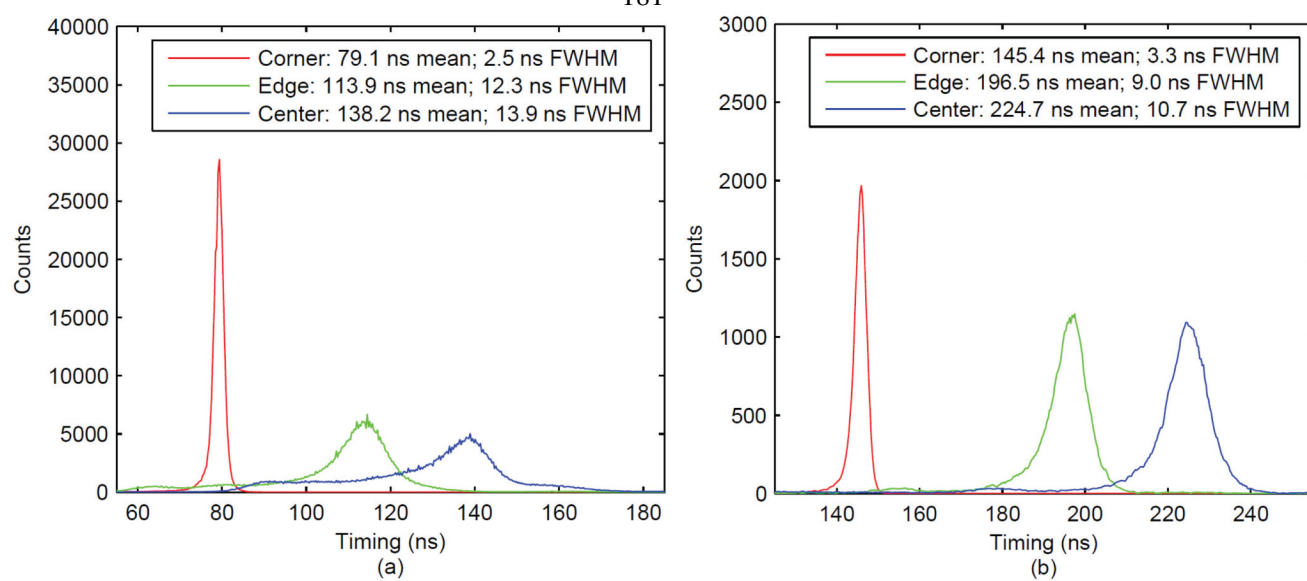
181

Figure 11.
Timing spectra obtained from 20×20 mm^2 PSAPD with CFD delay of (a) 45 ns and (b) 125 ns.
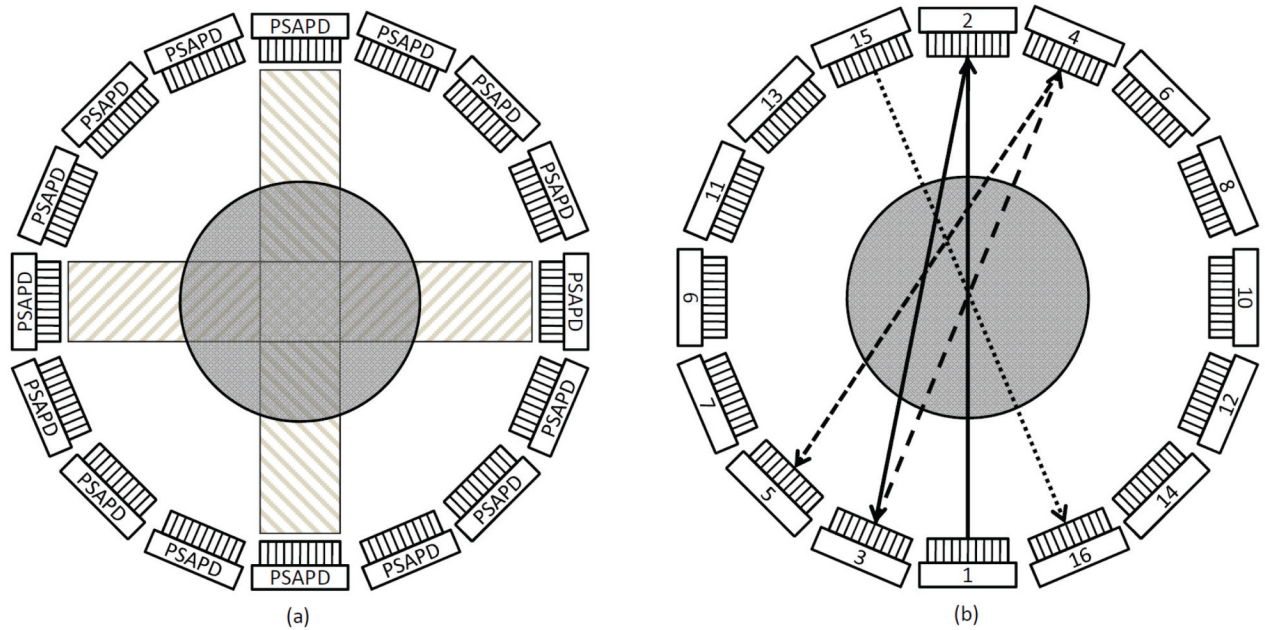
182

Figure 12.
Timing alignment scheme: to generate offset map for each individual PSAPD (a) and between
PSAPDs (b). The cylinders in (a) and (b) represent the sources. The rectangles in (a) represent
the regions covered by the opposing detector pairs. The lines with arrows in (b) show the
calibration sequence, starting from PSAPD #1 and ending at #16. The lines from #5 to #15 are
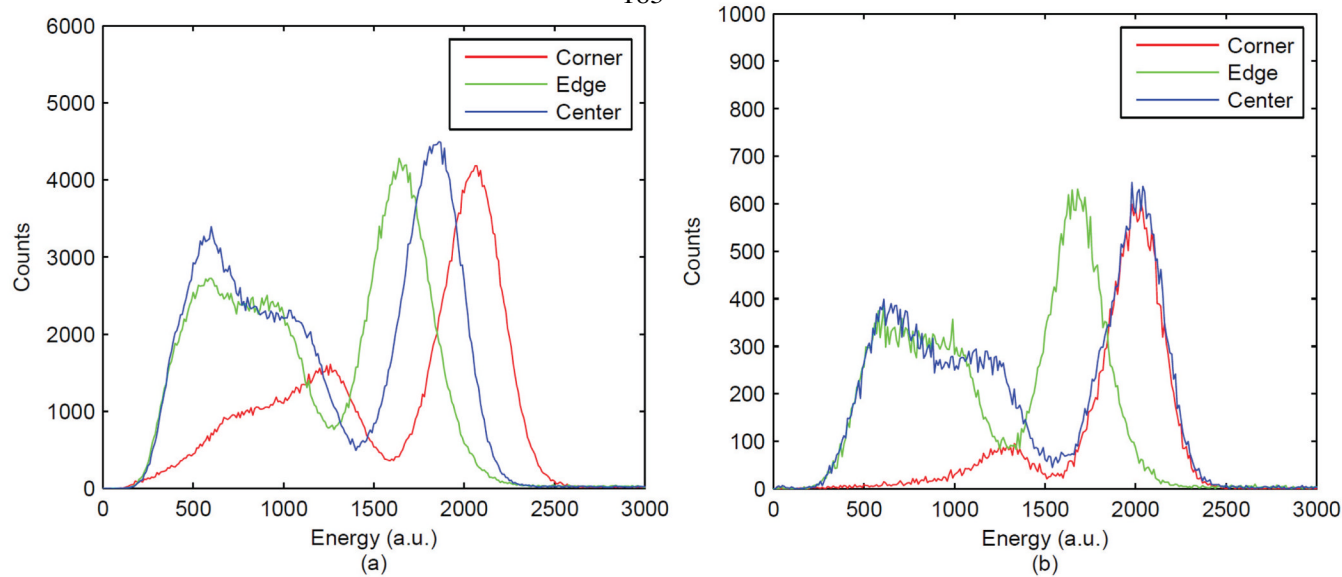omitted for clarity.

183

Figure 13.
Energy spectra obtained from 20×20 mm^2 PSAPD with CFD delay of (a) 45 ns and (b) 125 ns.

184

Table 1

Comparison of results (unit: ns)

	Individual crystal pairs							Whole arrays	
	Timing resolution (FWHM)				Timing centroid (mean of spectrum)			Timing resolution (FWHM)	Timing window (2τ)
	Mean	SD	Max	Min	SD	Max-Min			
No Correction	5.2	0.6	7.4	3.0	9.5	52.4		24.6	65.1
Method 1	5.2	0.6	7.4	3.0	2.3	9.7		9.5	22.0
Method 2	5.2	0.6	7.4	3.0	0.2	1.3		6.0	15.2

Appendix B

Receptor-targeted Iron Oxide Nanoparticles for Molecular MR Imaging of Inflamed Atherosclerotic Plaques

This paper describes work done in collaboration with Angelique Louie's group at the University of California, Davis. The work involved the development of a novel iron-oxide based nanoparticle that targets macrophages in vulnerable atherosclerotic plaques. Improved chemistry and functionalization (via sulfation) of the particle surface enabled improved plaque targeting compared to a first generation particle. I was responsible for the design, acquisition and analysis of the *in vivo* studies.
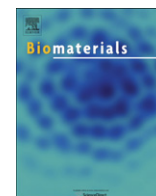
Receptor-targeted iron oxide nanoparticles for molecular MR imaging of inflamed atherosclerotic plaques

Chuqiao Tu [a], Thomas S.C. Ng [b], Hargun K. Sohi [b], Heather A. Palko [c], Adrian House [a], Russell E. Jacobs [b], Angelique Y. Louie [a,*]

[a] Department of Biomedical Engineering, University of California, Davis, CA 95616, USA
[b] Beckman Institute, California Institute of Technology, Pasadena, CA 91125, USA
[c] Department of Chemistry, University of California, Davis, CA 95616, USA

ARTICLE INFO

ABSTRACT

In a number of literature reports iron oxide nanoparticles have been investigated for use in imaging atherosclerotic plaques and found to accumulate in plaques via uptake by macrophages, which are critical in the process of atheroma initiation, propagation, and rupture. However, the uptake of these agents is non-specific; thus the labeling efficiency for plaques *in vivo* is not ideal. We have developed targeted agents to improve the efficiency for labeling macrophage-laden plaques. These probes are based on iron oxide nanoparticles coated with dextran sulfate, a ligand of macrophage scavenger receptor type A (SR-A). We have sulfated dextran-coated iron oxide nanoparticles (DIO) with sulfur trioxide, thereby targeting our nanoparticle imaging agents to SR-A. The sulfated DIO (SDIO) remained mono-dispersed and had an average hydrodynamic diameter of 62 nm, an r_1 relaxivity of 18.1 mM^{-1} s^{-1}, and an r_2 relaxivity of 95.8 mM^{-1} s^{-1} (37 °C, 1.4 T). Cell studies confirmed that these nanoparticles were nontoxic and specifically targeted to macrophages. *In vivo* MRI after intravenous injection of the contrast agent into an atherosclerotic mouse injury model showed substantial signal loss on the injured carotid at 4 and 24 h post-injection of SDIO. No discernable signal decrease was seen at the control carotid and only mild signal loss was observed for the injured carotid post-injection of non-sulfated DIO, indicating preferential uptake of the SDIO particles at the site of atherosclerotic plaque. These results indicate that SDIO can facilitate MRI detection and diagnosis of vulnerable plaques in atherosclerosis.

© 2011 Elsevier Ltd. All rights reserved.

1. Introduction

Cardiovascular disease (CVD) is the leading cause of death in the western world and its prevalence is expected to increase further during the next 3 decades [1]. Increasing evidence indicates that it is atherosclerotic plaque rupture rather than the severity of vessel occlusion that leads to major adverse events, such as stroke and myocardial infarction [2,3]. Early detection of unstable plaques would be of great value to guide treatment decisions, with the aim to decrease morbidity/mortality in affected patients. There is an intense focus in the field to identify specific biomarkers that indicate a plaque's risk for rupture and develop noninvasive methods to detect those markers [1,4,5]. Magnetic resonance imaging (MRI) has played a prominent role in anatomical and functional examinations of the major vessels; however, without signal enhancement, the technique lacks sufficient sensitivity to directly detect and identify biomarkers of interest [6,7]

Recent advances in the development of MRI contrast agents (CAs), which specifically target relevant biomarkers and enhance images to generate sufficient contrast in tissues and organs of interest, allow MRI to visualize molecules and molecular events occurring at a cellular level [6,8]. However, the amount of biomarkers in the cardiovascular system is usually expressed in the low nanomolar range ($\leq 10^{-9}$ mol/g of tissue), which is below the detection sensitivity of routinely used gadolinium chelates (10^{-7} mol/g of tissue). Particle-based technologies provide an effective method to concentrate signal-generating materials into a relatively small entity, which can greatly improve their detectability (10^{-10} - 10^{-11} mol/g of tissue) *in vivo* [7,9,10]. Moreover, the particle CAs have a large surface areas, allowing them to display more targeting ligands, further enriching the CAs at the region of interest (ROI).

Non-toxic and biocompatible iron oxide nanoparticles (IO NPs) have been widely used as MRI CAs in the clinic [11]. IO NPs,

* Corresponding author. Tel.: +1 530 7527134; fax: +1 530 7527156.
E-mail address: aylouie@ucdavis.edu (A.Y. Louie).

however, are generally non-specific; they show a differential distribution in the body based primarily on relative tissue permeability. We are interested in the development of IO NP CAs that target biomarkers of atherosclerotic plaques. In the search for markers to identify high-risk plaque, macrophages have been found to correlate with plaque stability — plaques with high macrophage content tend to be more unstable, and the distribution pattern for the macrophages can be indicative of degree of stability [12,13]. IO NPs have been used for MRI detection of plaques in pre-clinical experiments using different animal models of atherosclerosis, and the results showed that these particles accumulate in plaque macrophages [14]. However, the uptake of IO NPs by macrophages is non-specific through phagocytosis. This is an inefficient process that provides relatively weak contrast between the plaque and surrounding tissues [15]

We have previously developed CAs based on the scavenger receptor type A (SR-A) targeting ligands maleylated BSA and dextran sulfate [16–18]. SR-A is highly expressed on activated macrophages and not found on normal vessel walls [19]. These probes labeled atherosclerotic plaques with improved efficiency over non-targeted probes. However, it was difficult to obtain mono-dispersed IO NPs by synthesizing them using either dextran sulfate, or a combination of dextran sulfate and dextran, as a starting materials to form the coating [20]. In this work, we introduce a new synthetic method in which we coated IO NPs with dextran (DIO), then sulfated the dextran coating of the particles to make dextran sulfate coated IO NPs (SDIO). The ability of SDIO to target macrophages in vitro and to detect and access macrophages in atherosclerotic plaque in vivo was evaluated by MRI.

2. Materials and methods

2.1. Materials

Materials were obtained from commercial suppliers and used directly, unless otherwise noted. Dextran (from leuconostoc, average mol. wt. 9000–11,000) and ferric chloride hexahydrate ($FeCl_3 \cdot 6H_2O$, Fw 270.29 g/mol) were purchased from Sigma-Aldrich. Ferrous chloride tetrahydrate ($FeCl_2 \cdot 4H_2O$, Fw 198.81 g/mol) and dextran sulfate (sodium salt, prepared from dextran from leuconostoc SSP., average mol. wt. 5000) were acquired from Fluka. Ammonium hydroxide (28–30%), sodium bicarbonate and sodium hydroxide were provided by Fisher Scientific. Sulfur trioxide (SO_3) pyridine complex, sulfur trioxide DMF complex and 2-methyl-2-butene (2M2B) were purchased from Acros. Anhydrous formamide was purchased from MP, Biomedicals, LLC. Spectra/por® dialysis membrane (mol. wt. cut-off 50,000) was purchased from Spectrum Laboratories, Inc. P388D1 cells and RPMI-1640 medium were obtained from American Type Culture Collection (ATCC). Fetal bovine serum (FBS), L-glutamine, PBS (1X) and C_{12} − Resazurin were provided by GIBCO. Lipoprotein deficient bovine serum (LPDS) was obtained from Biomedical Technologies, Inc. (Stoughton, MA). Water was purified using a Millipore Milli-Q Synthesis purifier (18.0 MΩ cm, Barnstead).

2.2. Synthesis of dextran sulfate coated iron oxide nanoparticles

Dextran coated iron oxide nanoparticles (DIO) were synthesized as previously reported [20]. The DIO (200 mg) was dissolved in 10 mL of dry formamide. After complete dissolution, 2-methyl-2-butene (2M2B) (1.6 mL, 15 mmol) was slowly added to the flask under argon atmosphere and magnetic stirring. A SO_3–pyridine complex (0.32 g, 2 mmol) was rapidly added, and the reaction mixture was stirred at 30 °C under argon atmosphere for 2 h. The reaction was quenched by slowly pouring it into 7 mL of saturated sodium bicarbonate solution. After the final product was concentrated, the residue was dissolved in water and was dialyzed against deionized water in a dialysis bag with molecular weight (MW) cut-off of 50,000 Da for 72 h (8–10 changes of water). The solution was lyophilized to give a brown solid.

2.3. Characterization of SDIO

The iron oxide core size of SDIO and DIO were measured by transmission electron microscopy (TEM) on a Philips CM-12, operating at 80 kV. The average hydrodynamic particle size and size distribution of SDIO and DIO were measured using dynamic light scattering (DLS) with a Nanotrac 150 particle size analyzer (Microtrac, Inc., Montgomeryville, PA). The zeta potential (ζ) values of SDIO and DIO were measured by determining the electrophoretic mobility using a NICOMP™ 380

ZLS device (Particle Sizing Systems, Inc., Santa Barbara, CA, USA) in deionized water at room temperature. Elemental analysis was performed by Columbia Analytical Services of Tucson, Arizona. FT-IR spectra were collected on a Shimadzu IR Prestige 21 spectrophotometer.

Longitudinal (T_1) and transverse (T_2) relaxation times were measured at 60 MHz (1.4 T) and 37 °C on a Bruker Minispec mq60 (Bruker, Billerica, MA). Three stock solutions of SDIO were prepared by dissolving appropriate amounts of particles in pH 7.0 deionized water. The concentration of iron was determined by ICP-MS. The stock solutions were diluted to give three series of aqueous solutions with decreasing iron concentration (0.3 mL each). All solutions were prepared by weight. Iron concentrations were calculated based on the concentration of the stock solution and appropriate dilution factors. T_1 values were measured using an inversion recovery sequence with 10–15 data points and T_2 values were measured using a Carr−Purcell−Meiboom−Gill (CPMG) sequence with $\tau = 1$ ms, and 200 data points. Each solution was incubated at 37 °C for 10 min before measurement. The longitudinal (r_1) and transverse (r_2) relaxivity were determined as the slope of the line for plots of $1/T_1$ or $1/T_2$, respectively, against increasing iron concentration with a correlation coefficient greater than 0.99 [21]. The relaxivity of DIO was measured by the same procedure. The T_1 and T_2 relaxation times of cell lysates containing SDIO or DIO were also measured with the method described above.

2.4. Cell experiments

2.4.1. Cell culture

The P388D1 cells were maintained in tissue culture flasks (75 cm^2) in media (RPMI-1640 with 1% L-glutamine and 10% fetal bovine serum (FBS)) at 37 °C in a humidified environment of 5% CO_2 atmosphere. When the cells reached 80–90% confluence, the medium was removed. The cells were scraped down with a rubber policeman and used for either sub-culture or in vitro cell studies. All experiments were performed on cells that were passaged an equal number of times.

2.4.2. In vitro cellular uptake of SDIO and DIO

The P388D1 cells were plated to 60 mm diameter tissue culture dishes at 1×10^6 cells/mL of RPMI-1640 with 1% L-glutamine and 10% lipoprotein deficient bovine serum (LPDS) (2 mL per dish). The cells were maintained in media at 37 °C in a humidified environment of 5% CO_2 atmosphere overnight which allowed cells to adhere to the bottom of dishes.

Three stock solutions of SDIO or DIO were prepared by dissolving appropriate amount of particles in RPMI-1640 with 1% L-glutamine and 10% LPDS. The concentration of iron was determined by ICP-MS. The stock solutions were diluted with media to give series of three solutions with decreasing iron concentration. All solutions were prepared by weight and iron concentrations were calculated based on the concentration of the stock solution and appropriate dilution factors. The resultant media solutions of SDIO or DIO were incubated in 37 °C water bath for 20 min before use. After removal of maintenance media, the SDIO or DIO medium solutions were introduced to the cells and incubated at 37 °C in 5% CO_2 atmosphere for 2 h. After removal of the media, cells were washed with 1X PBS (37 °C) (3 × 2 mL for each dish, ~ 2 min for each washing). Deionized water was added in dishes (1.2 mL for each dish), and the freeze-thaw (30/20 min) method was repeated twice to lyse cells. The cell lysates were put into 1.5 mL conical tubes and lyophilized. Deionized water was added to the residue (0.3 mL each) to generate solutions for relaxation time measurement.

2.4.3. Specificity of uptake

To verify that cellular uptake was receptor-specific, competition experiments were conducted and characterized by relaxation times. The P388D1 cells were incubated with SDIO ([Fe] = 5.0×10^{-5} M) in the presence of competing dextran sulfate or non-competing dextran as control in 0, 0.02, 0.1, 0.4, 1, and 10-fold excess concentrations. Cells were incubated at 37 °C in a 5% CO_2 atmosphere for 2 h and then prepared for relaxation time measurement as described previously.

2.4.4. Cytotoxicity

Cytotoxicity of SDIO was evaluated with P388D1 cells using the C_{12} - Resazurin viability assays. P388D1 cells in RPMI-1640 were plated in 96-well dishes at a concentration of 1.1×10^4 cells per well. This places the cells at a density for linear growth rate which is optimal for the assay. After overnight incubation in 5% CO_2 atmosphere at 37 °C, the existing RPMI-1640 was replaced with fresh media containing varying amounts of SDIO. Cells were incubated with SDIO for either 4 or 24 h. The media were removed and cells were washed with 1X PBS three times, then media containing C_{12} - Resazurin (5 μM) was added. After incubation for 15 min for reduction of the compound, fluorescence was measured using a Safire^2 monochromator microplate reader (Tecan Austria G.M.B.H., Austria) with excitation of 563 nm and an emission of 587 nm. Samples were performed in triplicate to provide statistical significance.

2.5. Animal studies

2.5.1. Animal model

All animal experiments were performed under protocols approved by the Animal Care and Use Committee of the University of California, Davis and the

California Institute of Technology. Apo E$^{-/-}$ mice (12 weeks old, Jax West Laboratories, West Sacramento, CA) were used for the experiments. Either the right or left carotid artery of each mouse was ligated two weeks before imaging. Subsequent to ligation, mice were placed on a high fat diet (TD.88137, Harlan Laboratories Inc., Madison, WI). To perform the ligation a medial incision was made between the mandible and clavicle, exposing the glands and vessels of the neck. The carotid artery was singled out from the surrounding tissue, with much attention given to protecting and excluding the parallel-running vagus nerve. A 6/0 silk suture was threaded under the dorsal side of the carotid artery and was tied off to cause injury to the site. The procedure was concluded with five to six discontinuous 4/0 ethilon sutures to reconnect the skin of the original ventral incision. The mice were monitored twice a day for approximately four days to check for irritation and to administer analgesics when appropriate.

2.5.2. In vivo MRI

All images were acquired on a 7T (Bruker Biospec) small animal magnet using a home-built birdcage coil. For all time points, the animal was anesthetized with an 1.5% isofluorane:air mixture, kept at 35−37 °C with warm air flowing through the bore and the respiration was monitored (MP150, Biopac, Goleta, CA). After localizing the ROI around the neck using a RARE spin echo sequence (TR/TE = 4000/22 ms, matrix size = 128 × 128, FOV = 35.35 × 35.35 mm^2, slice thickness = 0.754 mm), the common carotid arteries were located with a time-of-flight angiography sequence with venous saturation (FL2D_ANGIO method, Paravision 4.0: TR/TE = 13.7/3.5 ms, matrix size = 150 × 100; zero-filled to 256 × 100, FOV = 30 × 20 mm^2, slice thickness = 0.754 mm). A gradient echo sequence was then utilized to visualize the uptake of SDIO/DIO particles (TR/TE = 1000/5 ms, F.A. = 35°, matrix size = 200 × 200; zero-filled to 256 × 200, FOV = 35.35 × 35.35 mm^2, slice thickness = 0.754 mm) at the region of the common carotid arteries. A set of pre-injection images was acquired one day prior to injection. For particle injection, 30 mg/kg Fe content of SDIO (n = 3) or DIO (n = 2) particles dissolved in saline were injected via the tail vein. The imaging protocol was then repeated at 4 h and 24 h post-injection.

2.5.3. MR images analysis

To analyze the acquired images, all gradient echo images were first reconstructed such that the intensity scaling and offset of all images for each mouse were equivalent. To compare particle uptake between timepoints and subjects, we define a contrast ratio (CR) metric as:

$$CR = \frac{\left| \frac{[I_{ligated}] - [I_{brain}]}{[I_{control}] - [I_{brain}]} \right|_i}{\left| \frac{[I_{ligated}] - [I_{brain}]}{[I_{control}] - [I_{brain}]} \right|_{prescan}} \qquad (1)$$

Where $I_{ligated}$ is the mean intensity of the region of interest (ROI) drawn around the ligated carotid artery, $I_{control}$ is the mean intensity of the ROI drawn around the contra-lateral carotid. I_{brain} is the mean intensity of the ROI drawn in the spinal cord at the same image slice as the other ROIs and i is either 4 or 24 h post-injection timepoints.

ROIs were drawn manually at slice levels approximately located at the common carotid arteries. These were matched between timepoints. Angiography images were used to guide ROI delineation around the carotid arteries. Because previous reports noted that the carotid vessels along with the wall are ~1 mm in diameter [22], all arterial ROIs had diameters of 1.5 mm. CR for SDIO injected mice and DIO injected mice were compared using a two-sided t-test in Microsoft Excel.

3. Results and discussion

3.1. Synthesis of SDIO

The DIO were synthesized according to our previously reported procedure [20]. The sulfation of polysaccharides has been reported via both heterogeneous and homogeneous synthesis pathways. Heterogeneous sulfation reactions with chlorosulfonic acid are subject to major drawbacks such as multiple and non-reproducible side reactions, presence of hazardous and non-reproducible sulfation rates and patterns, and backbone degradation. Homogeneous sulfation of dextran with nitrogen base complexes of sulfur trioxide in aprotic solvents are the preferred method; however, homogeneous reactions are still accompanied by some non-reproducible side reactions such as cleavage of labile functional groups and backbone degradation [23]. Our first effort to sulfate DIO followed literature methods, which performed sulfation of dextran with sulfur trioxide pyridine complex in dry formamide at room temperature [24]. However, the resultant

particles showed 2 size peaks with an average hydrodynamic diameter of 122 ± 97 nm. The sulfation reaction was reassessed under different synthetic conditions including varying temperatures, using sulfur trioxide DMF complex as sulfating agent, or using DMF as reaction solvent, yielding similar results. This indicates that although sulfation of dextran with nitrogen base complexes of sulfur trioxide is well-known [23], successful translation to a dextran coat on a nanoparticle is not trivial. The larger-sized peak may have been due to the depolymerization of dextran followed by aggregation of incompletely coated iron oxide nanoparticles.

Sulfur trioxide pyridine complex is made by dripping chlorine sulfate acid into dry pyridine at −15 °C [24]. However, the presence of pyridine may only partially limit the highly acidic character of chlorosulfonic acid, which is known to be responsible for multiple, undesirable, and non-reproducible side reactions such as cleavage of acid labile functional groups and partial depolymerization [25]. We therefore introduced an acid scavenger of a neutral nature, 2-methyl-2-butene (2M2B), into the reaction before the addition of sulfation agent, hypothesizing that this would clear the free acid produced in the system in a timely fashion and lead to a more efficient reaction, with diminished side reactions in the sulfation of dextran coat on IO NPs (Scheme 1) [25,26]. The purified, sulfated DIO were turned out to be mono-dispersed nanoparticles.

3.2. Characterization of SDIO

#### 3.2.1. SDIO formation verification

Successful sulfation was verified by infrared spectroscopy and elemental analysis of the purified particles. Compared to the infrared spectrum of DIO, new absorptions of S=O groups at 1234 cm^{-1} (asymmetrical stretch), 1011 cm^{-1} (symmetrical stretch), and 826 cm^{-1} (symmetrical C−O−S stretch) were observed, while the absorptions at 3426 cm^{-1} (O-H stretch) and 1026 cm^{-1} (C-O stretch) were decreased in the infrared spectrum of SDIO [24]. The emergence of sulfur (9.74%) and decrease of iron content (from 17.7% in DIO to 11.34% in SDIO) in SDIO further verified successful sulfation of DIO. The results from elemental analysis of sulfur content also showed that a 2 h reaction time was sufficient for the sulfation of DIO; longer reaction time did not appear to increase sulfation.

3.2.2. SDIO size, relaxivity and surface charge

SDIO has an average core size of 7−8 nm (Fig. 1a) and an average hydrodynamic diameter of 62.4 nm (Fig. 1b), an r_1 relaxivity of 18.1 mM^{-1} s^{-1}, and an r_2 relaxivity of 95.8 mM^{-1} s^{-1} (37 °C, 1.4 T) in pH 7.0 deionized water. The r_2 to r_1 ratio was 5.3, indicating that SDIO could be used, preferably, as a T_2-weighted MRI contrast agent.

The measured zeta potential (ζ) values were − 14.90 mV and − 40.05 mV for DIO and SDIO, respectively. Typically the ζ value reflects the electric charge on the particle surface and indicates the physical stability of dispersions and emulsions in a colloidal system [27]. Double layers with high ζ values would create powerful electrostatic repulsion and, consequently, prevent aggregation resulting from collisions caused by Brownian motion. In comparison with DIO, the ζ value of SDIO decreased by 25.15 mV, indicating a more stable dispersion and emulsification of SDIO in water. In practice, we found SDIO to be very stable, with a long shelf life in aqueous solution. We have not observed any properties to change (e.g. aggregation, size, and magnetic property) after benchtop storage for over a year at room temperature.

Dextran in DIO is coated on the surface of iron oxide core. Due to decreased access for hydroxyl groups that lay deeper in the polymer layer, we estimate that the degree of sulfation of outer polymer layer is greater than that of the inner polymer layer. This should be

189
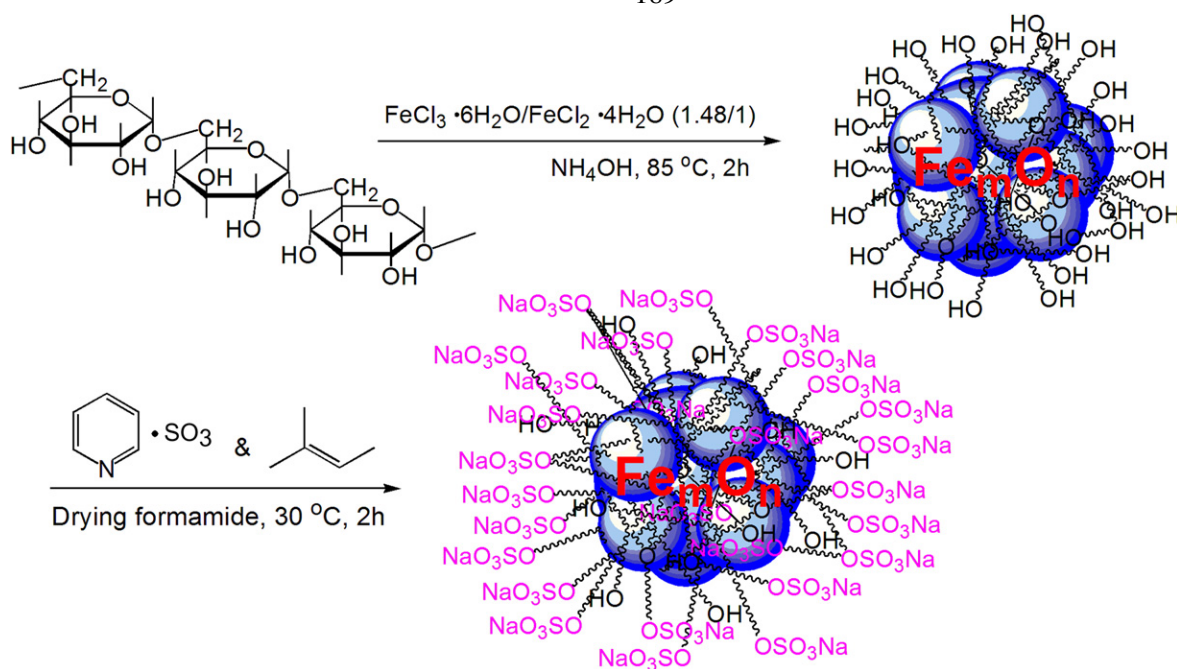
Scheme 1. Sulfation of dextran coated iron oxide nanoparticles.

ideal because the maximum sulfation of surface dextran can greatly increase the targeting ability of the nanoparticles to macrophages with less charge repulsion at the inner polymer layers that can affect size and MRI properties. Particle size was somewhat larger in comparison with that of non-sulfated DIO. This is likely due to the repulsion of negatively charged sulfate groups on the surface of SDIO. The r_1 and r_2 relaxivity values of SDIO were similar to those of DIO. This is not unexpected as the size of the iron oxide cores was similar for DIO and SDIO. Reproducibility of our method was validated by repeating the same reaction; running the reaction with a different scale of DIO; and using sulfur trioxide DMF complex as sulfation agent instead of sulfur trioxide pyridine complex. All of these reactions gave similar products, indicating that our sulfation procedure is reproducible and robust.

3.3. Cell experiments

3.3.1. SDIO targeting to macrophages P388D1

We selected SR-A as the target for our particles because it is highly expressed on activated macrophages in atheromas. SR-A recognizes and binds a number of polyanionic molecules, such as oxidized LDL, that contribute to the involvement of macrophages in the formation of plaques [28]. For example, experiments conducted on Apo E knockout (Apo E$^{-/-}$) mice demonstrated that knocking out SR-A resulted in a significant decrease in atherosclerotic plaque size [29]. To demonstrate targeting of SDIO to macrophages, we performed in vitro studies using P388D1 murine macrophage cells. Uptake of DIO was also performed as a control for comparison; the properties of the DIO particles were similar to those of the commercially available MRI CA Sinerem (Table 1) [30].

The T_2 values of the lysates of macrophages incubated with increasing concentrations of SDIO or DIO for 2 h are shown in Fig. 2. In comparison with DIO, the mean T_2 values were significantly lower for cell lysates incubated with SDIO at all concentrations. In comparison with the lysates of blank macrophages, SDIO at 5.0×10^{-5} M Fe significantly decreased T_2 by 70% (p value = 0.002), compared to a 20% T_2 decrease (p value = 0.03) for the same iron concentration of DIO, indicating that there was limited uptake of DIO compared to SDIO under the same conditions. This result was as expected because DIO is not a ligand of SR-A so it is not recognized
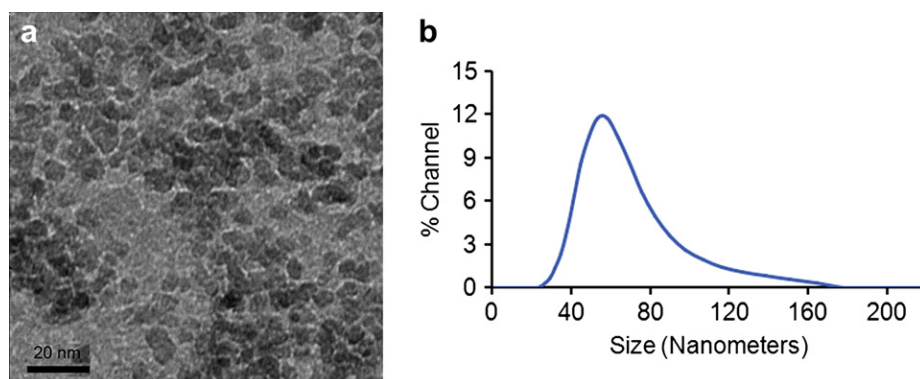

Fig. 1. (a) TEM, and (b) DLS of dextran sulfate coated iron oxide nanoparticles (SDIO).

Table 1
Characteristics of dextran sulfate coated iron oxide nanoparticles (SDIO), in comparison with dextran coated iron oxide nanoparticles (DIO) and commercially available dextran coated iron oxide nanoparticles (Sinerem).

Nanoparticles	Core size (nm)	Average hydrodynamic diameter (nm)	Relaxivity (mM^{-1} s^{-1}) (1.4 T, 37 °C)		% iron	ζ (mV)
			r_1	r_2		
SDIO	7–8	62.4	18.1	95.8	11.34	−40.05
DIO	7–8	42.4	15.7	89.2	17.7	−14.90
Sinerem	N/A	<50 nm	19.5[a]	87.6[a]	N/A	N/A

[a] 1.5 T, 37 °C.

by the receptor. Our results demonstrate that sulfation of DIO facilitates SR-A targeting, and greatly improves accumulation of the particles in macrophages over the non-targeted, dextran coated particles.

3.3.2. Receptor-mediated uptake of SDIO by macrophages P388D1

Specificity for the cellular uptake of SDIO was confirmed by competition studies in which cells were incubated with a fixed concentration of SDIO and increasing excess of unlabeled dextran sulfate (ligand of SR-A) or dextran (not a ligand of SR-A). If uptake of the agents was receptor-mediated, the excess unlabeled ligand should compete for binding to the receptors. Nonspecific uptake is strictly concentration-dependent and would not be affected by additional ligands in the solution [16,31]. Receptor-mediated uptake of SDIO was confirmed by the results seen in Fig. 3: increasing amounts of competitor, from 0.02 to 10-fold excess, strongly reduce uptake, while increasing amounts of excess dextran had little influence on the uptake, indicating that the uptake of SDIO by SR-A is a receptor-mediated process. To exclude the possibility that the reduced uptake of SDIO in the presence of dextran sulfate is caused by toxicity or any other influence of dextran sulfate on the cells themselves, dextran sulfate alone, at the same concentrations, was applied to P388D1 cells in culture and the cell viability was evaluated by the C$_{12}$ - Resazurin viability assay [32]. The average cell viability was above 96% after either 4 h or 24 h incubation of cells with the concentration of dextran sulfate varying from 0.04 to 10 × 10^{-3} M, indicating that the dextran sulfate is not toxic to mammalian cells (Supplementary Figure 1).

3.3.3. Cytotoxicity of SDIO to mammalian cells

As a preliminary assessment of SDIO's toxicity to cells, SDIO were applied to P388D1 cells in culture and the cell viability was evaluated by the C$_{12}$ - Resazurin viability assay [32]. Untreated cells served as negative control. The average cell viability is above 96% or

94% after 4 h or 24 h incubation with the particles varying from 0.02 to 5 × 10^{-3} M iron, respectively (Fig. 4). The result showed that SDIO at concentrations relevant for biological imaging do not have observable toxicity to mammalian cells. This is similar to the results for most of the *in vitro* cytotoxicity studies on iron oxide nanoparticles reported in the literature [33–36].

A major concern that limits the use of nanomaterials in clinic is the potential toxicity. The iron oxide nanoparticles have been used in the clinic due to their biocompatiblity. After injection the IO NPs are taken up in the liver and spleen where they are metabolized and broken down slowly to release free iron ions. The released iron ions are added to the body's iron stores and eventually incorporated by erythrocytes as hemoglobin [37]. Free iron ions could potentially be cytotoxic because of the catalytic function of iron in the production of reactive oxygen species (ROS), which in turn can cause lipid peroxidation, protein oxidation, and DNA damage. However, the body has the ability to process these released iron ions as indicated by iron's large median lethal dose (LD$_{50}$) of 450 mg/kg for oral ingestion in the rat model [10,14]. In fact, iron oxide nanoparticle MRI contrast agents have maintained an excellent safety record since they were approved for clinical use [37,38].

3.4. Animal studies

The Apo E$^{-/-}$ mouse is a widely accepted model for atherosclerosis. In practice, we found that ligation of carotid arteries was an effective method to generate macrophage-laden plaques [18]. The carotid artery is relatively superficial and more amenable to surgical procedures than the coronary artery. Therefore, to evaluate the preliminary *in vivo* capabilities of SDIO we utilized a carotid ligation model. A single carotid artery in the Apo E$^{-/-}$ mouse ($n = 5$) was ligated two weeks prior to the imaging study to induce atherosclerotic plaques. A T_2^*-weighted MRI with gradient echo sequence was utilized to visualize the uptake of SDIO and DIO
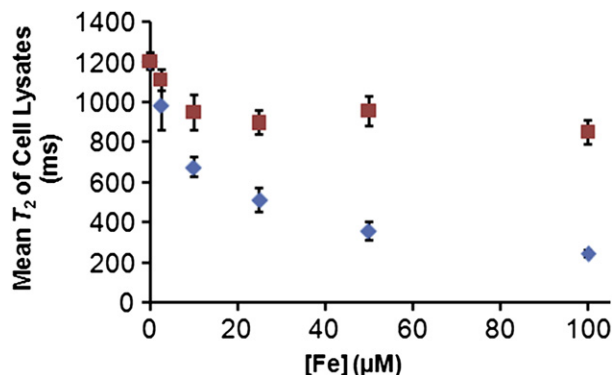
Fig. 2. Mean T_2 values of cell lysates incubated for 2 h with SDIO (◆) or DIO (■) of different iron concentrations.
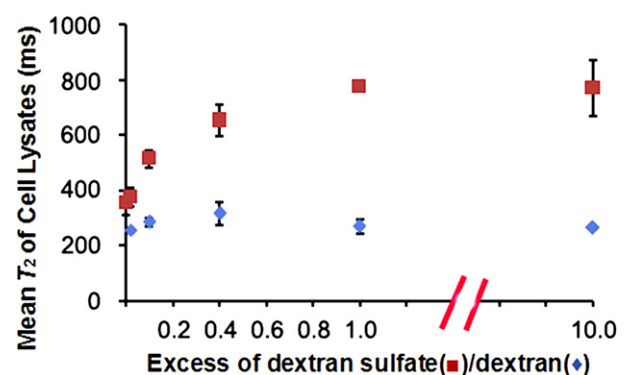
Fig. 3. Competitive uptake of SDIO ([Fe] = 5.0 × 10^{-5} M) and dextran sulfate (■), or dextran (◆) by P388D1 cells.
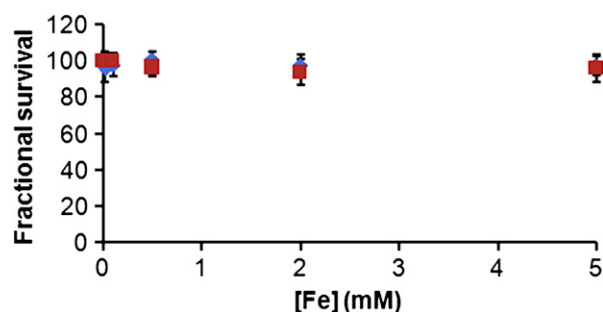
Fig. 4. Cell viability of P388D1 after 4- (◆), or 24 h (■) incubation with different concentrations of SDIO.

particles. Image slices from a representative mouse, matched at the same slice level of the mouse common carotid arteries over a 24-h time course are shown in Fig. 5a.

Because SDIO is a negative contrast agent, regions taking up SDIO produce a T_2^* susceptibility effect, appearing darker than areas without SDIO. The MR images displayed a sizeable decrease in the signal of the ligated carotid artery at 4 and 24 h compared to the pre-injection image. The result parallels that from the *in vitro* particle incubation time study that showed that T_2 values of the lysates of macrophages incubated with SDIO decreased substantially after a 4 h incubation time with little subsequent change (Supplementary Figure 2). No discernable signal decrease was seen on the control carotid artery. This suggests preferential uptake of the SDIO particles at the sites of atherosclerotic plaque. Image slices from a representative mouse injected with DIO particles is shown in Fig. 5b. Compared to SDIO injected animals, less signal intensity decrease was seen over time for the DIO injected subjects. Visualization of the volume regions above and below each slice depicted in Fig. 5, shown in Supplementary Videos 1-6, confirmed that the signal decreases observed were due to localization of contrast agent, and not in homogenities in endogenous signal between slices.

Supplementary video related to this article can be found at doi:10.1016.j.qdypi.2009.12.006.

To compare the relative uptake between SDIO and DIO particles in a more quantitative manner, we define a contrast ratio (CR) metric to measure the magnitude of signal decrease at the arterial
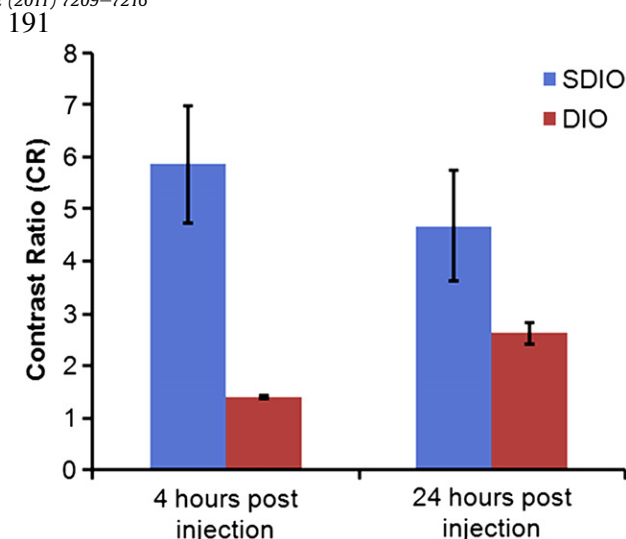

Fig. 6. Contrast Ratio between SDIO and DIO particle accumulation *in vivo*.

site. As seen in Fig. 6, the CR of SDIO injected mice were significantly higher than those of the DIO injected mice by 4 h post-injection (p value = 0.03). This suggests that at the same injected iron dose, SDIO accumulated preferentially compared to DIO particles at the site of atherosclerotic plaque. It should be noted that the ROIs delineated included the signal contribution of particles in the blood. We normalize for this effect by comparing between the left and right carotids, which factors out the signal contribution due to blood borne particles.

Iron oxide nanoparticle-enhanced MRI has been reported to be able to identify atherosclerotic plaques in both *in vivo* animal and human studies [14]. However, the non-specific contrast agents are taken up by activated macrophages in vulnerable plaques via phagocytosis, pinocytosis or fluid-phase transport, which are inefficient processes [15]. As a result, direct visualization of atherosclerotic plaques often required relatively large amounts of nanoparticles [14,39]. A tissue-specific contrast agent would allow for an improved identification of these lesions [38,40]. Active targeting of nanoparticles can be achieved by decorating them with a ligand against a known marker associated with lesions. Our *in vivo* MRI images revealed that at 4 h post-injection, targeted SDIO
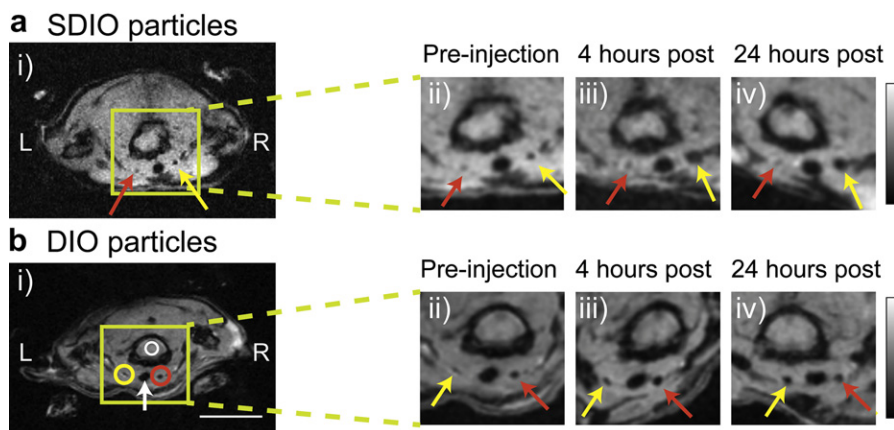

Fig. 5. Signal change in MRI over time after SDIO (a) or DIO (b) injection. The ligated carotid artery is denoted by the yellow arrow and the control carotid artery is denoted by the red arrow. Circles indicate the ROI measures used to derive the contrast ratio (CR) metric. To facilitate comparison, the magnified images in carotid areas were first rotated in plane so all timepoints in the orientation. They were then zero-filled by a factor of 2 and then smoothed with a 2×2 Gaussian filter. (Scale bar = 10 mm, both scale bar and intensity bar apply to the whole animal images only. L = left, R = right, green box shows magnification area, white arrow denotes the trachea). (For interpretation of the references to colour in this figure legend, the reader is referred to the web version of this article.)

provided a 4-fold increase in the contrast ratio compared to non-targeted DIO. The contrast ratio metric was used to account for differences in anatomy and physiology between subjects. Comparing the signal decrease between the ligated and control artery region normalizes the metric and allows cross comparisons over timepoints and between subjects. It should be noted that the ROIs delineated included the signal contribution of particles in the blood. We normalize for this effect by comparing between the left and right carotids, which factors out the signal contribution due to blood borne particles. Comparison between the CR of SDIO versus DIO injected mice (Fig. 6) suggests a time-dependence for optimal SDIO uptake. This is likely to be a function of the degree of vulnerability of the plaque at the local site as well as the general pharmacokinetics of the particles. Future studies will aim to correlate this with *ex-vivo* assays to further understand the mechanism of particle accumulation.

We have previously shown the SR-A is a viable target for labeling macrophages and atherosclerotic plaques [16,17]. Recently, micelles containing gadolinium chelates and antibodies against SR-A have been synthesized and applied to MRI of aortic plaques in Apo E$^{-/-}$ mice. In vivo MRI revealed that at 24 h post-injection, targeted micelles provided a 79% increase in signal intensity of atherosclerotic aortas compared with 34% using non-targeted micelles, and no enhancement occurred using Gd-DTPA. Uptake of the micelles was shown, through competition experiments, to be a receptor-mediated process [41]. However, the potential immunogenicity of antibodies and cost to generate them in a quantity may limit the use of immunomicelles clinically [10]. Small molecules or polymers are alternatives to antibodies [42]. SR-A recognizes a wide range of ligands that are polyanionic, though not all polyanionic molecules. Our results show that sulfation of dextran coated IO NPs greatly increased the negative charges on the particle surface (high negative ζ value); this allowed the particles to be recognized by SR-A and accumulate at the injured carotid artery in vivo. Competition studies support that the particles were taken up by a receptor-mediated uptake and not merely due to non-specific electrostatic association.

Macrophages and macrophage scavenger receptors play a key role in the pathogenesis of atherosclerosis. Macrophages are present through all stages of atherosclerosis development, from the initiation of plaques through the formation of complex plaques containing foam cells, necrotic debris, and thrombi, and have been specifically associated with plaque stability—high densities of macrophages correlate with vulnerability to rupture [5,13]. Our results show that SDIO can be recognized and specifically taken up by macrophages via scavenger receptor. Their specific accumulation at the injured carotid, but not the control carotid, suggests the potential to use SDIO with MRI to detect and distinguish inflamed atherosclerotic plaques.

4. Conclusion

The use of MRI is a well-established means for injury and disease diagnosis on the anatomic scale. Current advances in targeted contrast agents allow researchers to gather *in vivo* anatomic and molecular information simultaneously. IO NPs modified to target various moieties in atherosclerotic plaques have demonstrated their utility as an important tool for enhancing magnetic resonance detection of atherosclerosis at the anatomical, cellular and molecular levels [43]. However, to date, reports of targeted MRI of macrophages, a key component in the formation and development of vulnerable plaques, are relatively rare. In this paper, we sulfated dextran coated IO NPs and therefore targeted the nanoparticles to scavenger receptors on macrophages. SDIO has a high r_2 value of 95.8 mM^{-1} s^{-1} and an r_2/r_1 ratio of 5.3 (37 °C, 1.4 T),

therefore acts as an efficient T_2-weighted MRI contrast agent. We demonstrate that SDIO nanoparticles are specifically and avidly taken up by macrophages via a receptor-mediated process that labels macrophages much more efficiently than non-sulfated analogues, and produces distinct contrast in both *in vitro* and *in vivo* T_2^*-weighted MRI images. High macrophage density has been associated with atherosclerotic plaques vulnerable to rupture. Thus, the specific targeting of macrophages with the MR nanoparticle imaging agent SDIO demonstrates the potential for SDIO to facilitate detection and diagnosis plaque stability with *in vivo* MRI.

Appendix. Supplementary material

Supplementary data associated with this article can be found, in the online version, at doi:10.1016/j.biomaterials.2011.06.026 .

References

[1] Fuster V, Lois F, Franco M. Early identification of atherosclerotic disease by noninvasive imaging. Nat Rev Cardiol 2010;7:327–33.
[2] Wickline SA, Neubauer AM, Winter PM, Caruthers SD, Lanza GM. Molecular imaging and therapy of atherosclerosis with targeted nanoparticles. J Magn Reson Imaging 2007;25:667–80.
[3] Cyrus T, Lanza GM, Wickline SA. Molecular imaging by cardiovascular MR. J Cardiovasc Magn Reson 2007;9:827–43.
[4] Rudd JHF, Hyafil F, Fayad ZA. Inflammation imaging in atherosclerosis. Arterioscler Thromb Vasc Biol 2009;29:1009–16.
[5] Shaw SY. Molecular imaging in cardiovascular disease: targets and opportunities. Nat Rev Cardiol 2009;6:569–79.
[6] Winter PM, Caruthers SD, Lanza GM, Wickline SA. Quantitative cardiovascular magnetic resonance for molecular imaging. J Cardiov Magn Reson 2010;12. Article Number: 62.
[7] Sosnovik DE, Nahrendorf M, Weissleder R. Molecular magnetic resonance imaging in cardiovascular medicine. Circulation 2007;115:2076–86.
[8] Terreno E, Castelli DD, Viale A, Aime S. Challenges for molecular magnetic resonance imaging. Chem Rev 2010;110:3019–42.
[9] Geraldes C, Laurent S. Classification and basic properties of contrast agents for magnetic resonance imaging. Contrast Media Mol Imaging 2009;4:1–23.
[10] Cormode DP, Skajaa T, Fayad ZA, Mulder WJM. Nanotechnology in medical imaging probe design and applications. Arterioscler Thromb Vasc Biol 2009; 29:992–1000.
[11] Qiao RR, Yang CH, Gao MY. Superparamagnetic iron oxide nanoparticles: from preparations to in vivo MRI applications. J Mater Chem 2009;19:6274–93.
[12] Croons V, Martinet W, De Meyer GRY. Selective removal of macrophages in atherosclerotic plaques as a pharmacological approach for plaque stabilization: benefits vs. potential complications. Curr Vasc Pharmacol 2010;8: 495–508.
[13] Osborn EA, Jaffer FA. Advances in molecular imaging of atherosclerotic vascular disease. Curr Opin Cardiol 2008;23:620–8.
[14] Tang TY, Muller KH, Graves MJ, Li ZY, Walsh SR, Young V, et al. Iron oxide particles for atheroma imaging. Arterioscler Thromb Vasc Biol 2009;29: 1001–8.
[15] Sadat U, Li ZY, Graves MJ, Tang TY, Gillard JH. Noninvasive imaging of atheromatous carotid plaques. Nat Clin Pract Cardiovasc Med 2009;6:200–9.
[16] Gustafsson B, Youens S, Louie AY. Development of contrast agents targeted to macrophage scavenger receptors for MRI of vascular inflammation. Bioconjug Chem 2006;17:538–47.
[17] Tu CQ, Ma XC, Pantazis P, Kauzlarich SM, Louie AY. Paramagnetic, silicon quantum dots for magnetic resonance and two-photon imaging of macrophages. J Am Chem Soc 2010;132:2016–23.
[18] Jarrett BR, Correa C, Ma KL, Louie AY. In vivo mapping of vascular inflammation using multimodal imaging. PLoS One 2010;5. Article Number: e13254.
[19] de Winther MPJ, van Dijk KW, Havekes LM, Hofker MH. Macrophage scavenger receptor class A - A multifunctional receptor in atherosclerosis. Arterioscler Thromb Vasc Biol 2000;20:290–7.

[20] Jarrett BR, Frendo M, Vogan J, Louie AY. Size-controlled synthesis of dextran sulfate coated iron oxide nanoparticles for magnetic resonance imaging. Nanotechnology 2007;18. Article Number: 035603.

[21] Tu CQ, Louie AY. Photochromically-controlled, reversibly-activated MRI and optical contrast agent. Chem Commun; 2007:1331–3.

[22] Kumar A, Hoover JL, Simmons CA, Lindner V, Shebuski RJ. Remodeling and neointimal formation in the carotid artery of normal and P-selectin-deficient mice. Circulation 1997;96:4333–42.

[23] Heinze T, Liebert T, Heublein B, Hornig S. Functional polymers based on dextran. Adv Polym Sci 2006;205:199–291.

[24] Mahner C, Lechner MD, Nordmeier E. Synthesis and characterisation of dextran and pullulan sulphate. Carbohydr Res 2001;331:203–8.

[25] Papy-Garcia D, Barbier-Chassefiere V, Rouet V, Kerros ME, Klochendler C, Tournaire MC, et al. Nondegradative sulfation of polysaccharides. synthesis and structure characterization of biologically active heparan sulfate mimetics. Macromolecules 2005;38:4647–54.

[26] Wondraczek H, Pfeifer A, Heinze T. Synthetic photocrosslinkable polysaccharide sulfates. Eur Polym J 2010;46:1688–95.

[27] Obeidat WM, Schwabe K, Muller RH, Keck CM. Preservation of nanostructured lipid carriers (NLC). Eur J Pharm Biopharm 2010;76:56–67.

[28] Greaves DR, Gordon S. The macrophage scavenger receptor at 30 years of age: current knowledge and future challenges. J Lipid Res 2009;50:S282–6.

[29] Babaev VR, Gleaves LA, Carter KJ, Suzuki H, Kodama T, Fazio S, et al. Reduced atherosclerotic lesions in mice deficient for total or macrophage-specific expression of scavenger receptor-A. Arterioscler Thromb Vasc Biol 2000;20:2593–9.

[30] Gossuin Y, Gillis P, Hocq A, Vuong QL, Roch A. Magnetic resonance relaxation properties of superparamagnetic particles. Wiley Interdiscip Rev Nanomed Nanobiotechnol 2009;1:299–310.

[31] Tu C, Nagao R, Louie AY. Multimodal magnetic-resonance/optical-imaging contrast agent sensitive to NADH. Angew Chem Int Ed Engl 2009;48:6547–51.

[32] O'Brien J, Wilson I, Orton T, Pognan F. Investigation of the Alamar Blue (resazurin) fluorescent dye for the assessment of mammalian cell cytotoxicity. Eur J Biochem 2000;267:5421–6.

[33] Muller K, Skepper JN, Posfai M, Trivedi R, Howarth S, Corot C, et al. Effect of ultrasmall superparamagnetic iron oxide nanoparticles (Ferumoxtran-10) on human monocyie-macrophages in vitro. Biomaterials 2007;28:1629–42.

[34] Metz S, Bonaterra G, Rudelius M, Settles M, Rummeny EJ, Daldrup-Link HE. Capacity of human monocytes to phagocytose approved iron oxide MR contrast agents in vitro. Eur Radiol 2004;14:1851–8.

[35] Schulze E, Ferrucci JT, Poss K, Lapointe L, Bogdanova A, Weissleder R. Cellular uptake and trafficking of a prototypical magnetic iron-oxide label in-vitro. Invest Radiol 1995;30:604–10.

[36] Mailander V, Lorenz MR, Holzapfel V, Musyanovych A, Fuchs K, Wiesneth M, et al. Carboxylated superparamagnetic iron oxide particles label cells intracellularly without transfection agents. Mol Imaging Biol 2008;10:138–46.

[37] Sun C, Lee JSH, Zhang MQ. Magnetic nanoparticles in MR imaging and drug delivery. Adv Drug Deliv Rev 2008;60:1252–65.

[38] Sosnovik DE, Caravan P. Molecular MRI of atherosclerotic plaque with targeted contrast agents. Curr Cardiovasc Imaging Rep 2009;2:87–94.

[39] Nahrendorf M, Zhang HW, Hembrador S, Panizzi P, Sosnovik DE, Aikawa E, et al. Nanoparticle PET-CT imaging of macrophages in inflammatory atherosclerosis. Circulation 2008;117:379–87.

[40] Uppal R, Caravan P. Targeted probes for cardiovascular MRI. Future Med Chem 2010;2:451–70.

[41] Amirbekian V, Lipinski MJ, Briley-Saebo KC, Amirbekian S, Aguinaldo JGS, Weinreb DB, et al. Detecting and assessing macrophages in vivo to evaluate atherosclerosis noninvasively using molecular MRI. Proc Natl Acad Sci U S A 2007;104:961–6.

[42] Choudhury RP, Fisher EA. Molecular imaging in atherosclerosis, thrombosis, and vascular inflammation. Arterioscler Thromb Vasc Biol 2009;29:983–91.

[43] Thorek DLJ, Chen A, Czupryna J, Tsourkas A. Superparamagnetic iron oxide nanoparticle probes for molecular imaging. Ann Biomed Eng 2006;34:23–38.

Receptor-targeted Iron Oxide Nanoparticles for Molecular MR Imaging of Inflamed Atherosclerotic Plaques

Chuqiao Tu [a], Thomas S.C. Ng [b], Hargun Sohi [b], Heather Palko [c], Adrian House [a],

Russell E. Jacobs [b], and Angelique Y. Louie [a,*]

[a] Department of Biomedical Engineering, [c] Department of Chemistry, University of California, Davis, CA 95616, USA. [b] Beckman Institute, California Institute of Technology, Pasadena, CA 91125, USA.

Supporting Information

Table of Contents

Captions of videos 1-6

Supplementary video 1.

Pre-injection MRI of neck/carotid region prior to the administration of SDIO probes. Slices above and below the plane of Figure 5ai are provided in the video clip. Figure 5ai is the center slice of the volume set, denoted by frames containing white borders. Arrows are present to denote the ligated (yellow) right carotid artery and the non-ligated (red) left carotid artery. Video frames are zero-filled by a factor of 4 in plane and by a factor of 8 across slices to facilitate visualization of the volume.

Supplementary video 2

MRI of neck/carotid region 4 hours post injection of SDIO probes. Slices above and below the plane of Figure 5aiii are provided in the video clip. Slices matching Figure 5aiii are framed by white borders. As per Figure 5ai, the central slice of this volume is matched to the central slice Supplementary video 2. Arrows are present to denote the ligated (yellow) right carotid artery and the non-ligated (red) left carotid artery. Video frames are zero-filled by a factor of 4 in plane and by a factor of 8 across slices to facilitate visualization of the volume.

Supplementary video 3

MRI of neck/carotid region 24 hours post injection of SDIO probes. Slices above and below the plane of Figure 5aiv are provided in the video clip. Slices matching Figure 5aiv are framed by white borders. As per Figure 5ai, the central slice of this volume is matched to the central slice Supplementary video 3. Arrows are present to denote the

ligated (yellow) right carotid artery and the non-ligated (red) left carotid artery. Video frames are zero-filled by a factor of 4 in plane and by a factor of 8 across slices to facilitate visualization of the volume.
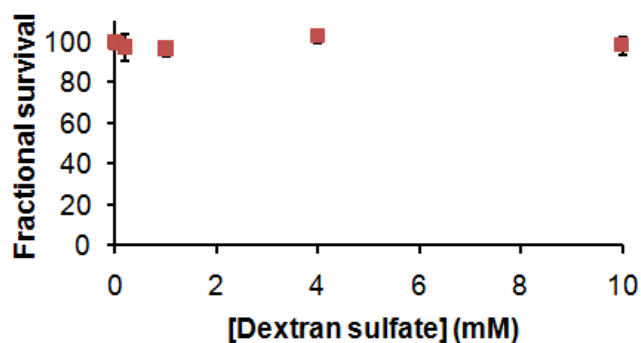
Supplementary video 4

Pre-injection MRI of neck/carotid region prior to the administration of DIO probes. Slices above and below the plane of Figure 5bi are provided in the video clip. Figure 5bi is the center slice of the volume set, denoted by frames containing white borders. Arrows are present to denote the ligated (yellow) right carotid artery and the non-ligated (red) left carotid artery. Video frames are zero-filled by a factor of 4 in plane and by a factor of 8 across slices to facilitate visualization of the volume.
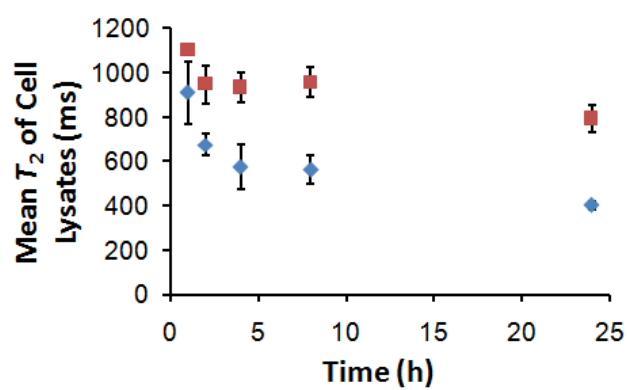
Supplementary video 5

MRI of neck/carotid region 4 hours post injection of DIO probes. Slices above and below the plane of Figure 5biii are provided in the video clip. Slices matching Figure 5biii are framed by white borders. As per Figure 5bi, the central slice of this volume is matched to the central slice Supplementary video 5. Arrows are present to denote the ligated (yellow) right carotid artery and the non-ligated (red) left carotid artery. Video frames are zero-filled by a factor of 2 in plane and by a factor of 8 across slices to facilitate visualization of the volume.

Supplementary video 6

MRI of neck/carotid region 24 hours post injection of DIO probes. Slices above and below the plane of Figure 5biv are provided in the video clip. Slices matching Figure 5biv are framed by white borders. As per Figure 5bi, the central slice of this volume is matched to the central slice Supplementary video 5. Arrows are present to denote the ligated (yellow) right carotid artery and the non-ligated (red) left carotid artery. Video frames are zero-filled by a factor of 2 in plane and by a factor of 8 across slices to facilitate visualization of the volume.

Supplementary Fig. 1. Cell viability of P388D1 after 24-h incubation with different concentrations of dextran sulfate.

Supplementary Fig. 2. Mean T_2 values of cell lysates incubated with 1.0×10^{-5} M iron of SDIO (♦) or DIO (■) for different incubation times.

Appendix C

Cooccurence Matrices to Compare Multimodal Image Datasets: Further Considerations

A cooccurence matrix method was proposed in section 3.4 to compare multimodal imaging datasets voxel-by-voxel. Here we explored the effects of image spatial resolution disparity (as is present between PET and MRI images) on analysis made using this method and compared it with the direct voxel-by-voxel comparison method by simulation.

C.1   Methods

ADC maps derived from diffusion MRI data acquired for studies described in chapter 5 were used as the baseline *high-resolution* scans. For simulation purposes, we consider only the two-dimensional case and only for the tumor ROI.

C.1.1   Effects of Spatial Resolution on Voxel-by-voxel Analysis

Datasets that simultate those encountered in PET were generated by applying two-dimensional Gaussian filters of varying FWHM on the baseline dataset. In the first condition, we applied a spatially invariant filter on the baseline image. The effect of increasing FWHM (i.e.PSF, FWHM = 0–5 mm) on voxel-by-voxel comparison metrics were examined. Next, we filtered the image with a spatially variant filter to simultate spatially varying PSFs usually encountered in PET. FWHM as a function of radial distance from the center was determined from measurements made with the PET/MRI scanner [198]. FWHM at radial distances of <10 mm, the outer limit of the measurements,

were calculated from a quadratic fit from the data. The maximum FWHM from this fit was applied to radial distances of >10 mm. This represented a best case scenario as spatial resolution typically worsens farther away from the system's center [291]. Gaussian filtering was applied voxel-by-voxel using a nonlinear sliding window algorithm available as part of the MATLAB image processing package.

There are instances where we are interested in comparing regions of low signal in one modality with high signal in the other modality. To investigate this scenario, we generated blurred images from baseline images that have been inverted. An inverted baseline image, $Baseline_{inverted}$ was generated from the original baseline image $Baseline_{original}$ by

$$Baseline_{inverted}(i,j) = \left[Max(Baseline_{original}) - Baseline_{original}(i,j)\right] + Min(Baseline_{original}),$$

(C.1)

i, j are voxels indices within the tumor ROI.

Two metrics, the Pearson's correlation coefficient (PCC) and the concordance correlation coefficient (CCC) were calculated for voxel-by-voxel comparisons between baseline and Gaussian filtered images.

C.1.2   Cooccurence Matrix Analysis

The cooccurence matrix method was described in detail in section 3.4.3.4. Here, we examined how two variables present in this method may affect analysis.

C.1.2.1   PSF Window

One variable that may affect analysis is the PSF window considered around each voxel. cooccurence matrices were calculated with different PSF windows ($|\Delta x|$, $|\Delta y| = 0$–5 mm), comparing the baseline image with four datasets:

1. The baseline image itself, as control (control matrix).

2. Baseline image blurred with static Gaussian filter (FWHM = 1.5 mm) to simulate the PET/MRI system.

3. Baseline image blurred with static Gaussian filter (FWHM = 2.2 mm) to simulate the microPET system.

4. Baseline image blurred with the spatially variant Gaussian filter to simulate actual PET systems.

Cooccurence matrices were compared to the control matrix using CCC to evaluate the method's ability to compare data with different spatial resolutions. We repeated the analysis by comparing baseline images with inverted blurred images.

C.1.2.2 Binning method

The cooccurence matrix is based on joint 2D histograms. Thus, an important parameter for this method is the choice of bins. We explored the robustness of the technique by comparing CCC values returned from matrices calculated with the following bin locations:

1. Minimum value = 0, maximum value = 65th percentile of tumor ADC values.

2. Minimum value = 0, maximum value = 75th percentile of tumor ADC values.

3. Minimum value = 0, maximum value = 85th percentile of tumor ADC values.

4. Minimum value = 0, maximum value = 95th percentile of tumor ADC values.

5. Minimum value = 0, maximum value = 100th percentile of tumor ADC values.

The number of histogram bins was set at 22. This was the average number returned from an optimal binning algorithm applied to the ADC data [292].

All simulations were performed in MATLAB. ADC images from three different animals acquired during different imaging sessions were used for the simulations.

C.2   Results and Discussion

C.2.1   Direct Voxel-by-voxel Comparison of PET and MRI Images is not Ideal

Voxel-by-voxel comparisons between baseline images and images blurred with a static and spatially varying Gaussian filter (which forms the ideal case) are shown in figure C.1. Image details, such

as the shape of the central fluid region in the tumor were lost upon filtering. Less details were lost when a spatially varying filter was used compared to the static filter. Visual inspection of the voxel-by-voxel plots did not show any obvious correlation between the baseline and blurred datasets. This was reflected in the correlation metrics. PCC and CCCs from the blurred to baseline comparisons decreased signficantly from unity (PCC: -30%–50%, CCC: –60%–70%). This indicated that direct voxel-by-voxel comparisons of PET and MRI data is not optimal and can mask structures that may be correlated between the two modalities.

The effect of PSF size was examined by varying the filter FWHM (figure C.2). For the positive contrast comparison, PCC and CCC were dramatically reduced when FWHM >1 mm, the nominal resolution achievable by PET. The correlation drop off is more dramatic in the inverted comparison case: PCC and CCC were already attenuated for mouse 2 and mouse 3 with a filter of FWHM = 0.01 mm. This is expected, since Gaussian filters cause spillover of high voxel intensities into areas of lower voxel intensities.

## C.2.2 Cooccurence Matrix Comparison Provides an Reasonable Alternative to Direct Voxel Comparison

Example cooccurence matrices for baseline-baseline and baseline-spatially variant filtered datasets are shown in figure C.3. The general pattern between the two matrices are similar. Slight differences between the two matrices are present. For example, a small portion of the lower ADC voxels on the blurred image cooccur with high ADC voxels on the baseline image. We quantified this difference by calculating the CCC for different binning methods at different PSF windows. The results for baseline/positive contrast and baseline/inverted contrast are shown in figure C.4.

A few trends were observed. Firstly, at the optimal PSF window and binning condition (~1 mm window, bin location condition 2), $Baseline_{original}$ vs. $Baseline_{original}$-blurred matrices were consistently similar to $Baseline_{original}$ vs. $Baseline_{original}$ matrices for different animals. This was demonstrated by the high (>0.7) CCC values at the optimal condition. This suggests that cooccurence matrices are able to recover image patterns that are obscured by blurring.

Secondly, cooccurence matrices calculated for $Baseline_{original}$ vs. $Baseline_{original}$-blurred images showed consistently higher CCC values compared to $Baseline_{original}$ vs. $Baseline_{inverted}$-blurred
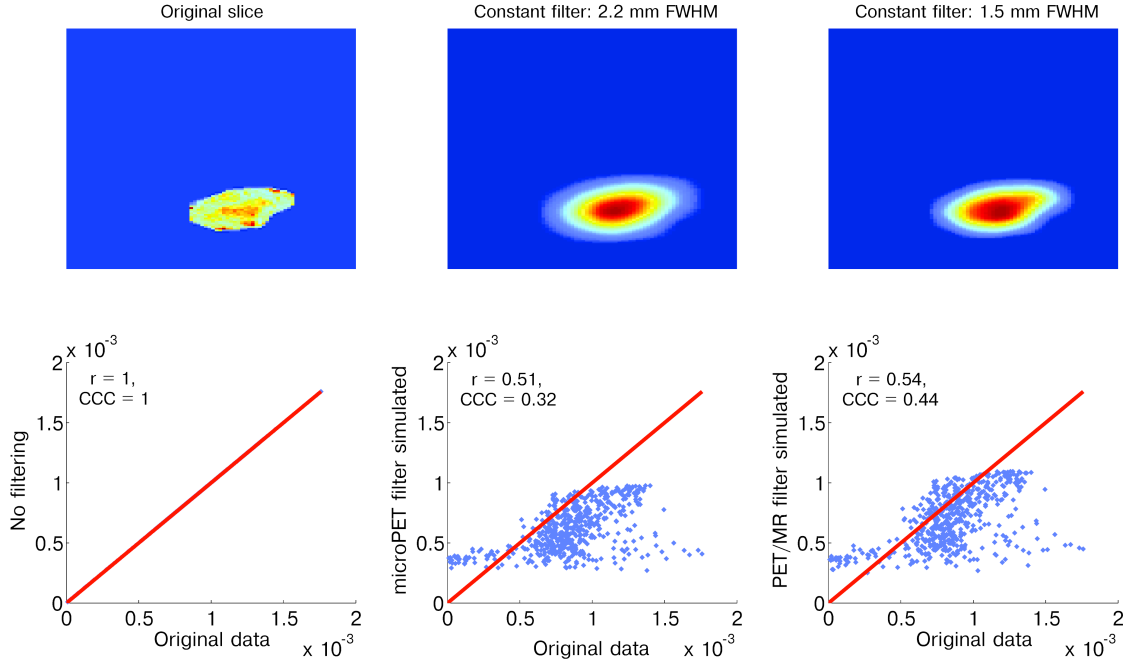
(a) Voxel-by-voxel comparisons of images filtered by spatially invariant Gaussian functions. Scatterplots do not reveal any obvious correlation between the datasets.
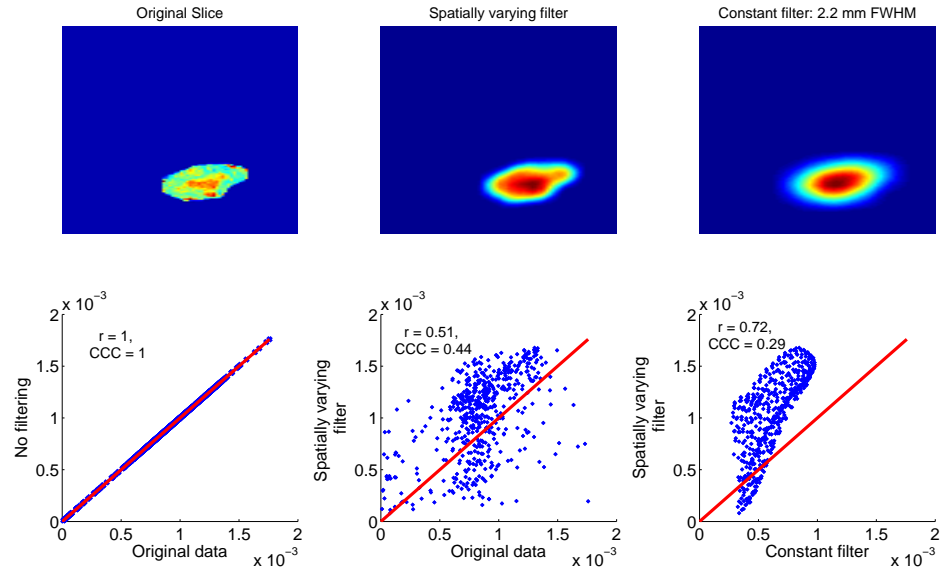

(b) Voxel-by-voxel comparisons of images filtered spatially variant Gaussian functions. Although tumor details were less obscured, scatterplots still do not reveal any obvious correlation between the datasets.

Figure C.1: Voxel-by-voxel comparisons between images with different spatial resolutions for a single ADC dataset. Gaussian blurring drastically reduces image detail and obscures correlation by direct voxel analysis.
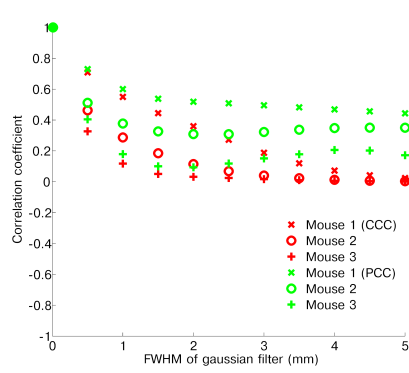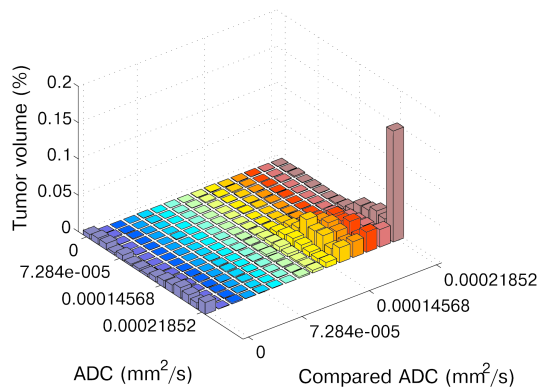
(a) Correlation of baseline and blurred data. A coefficient of 1 would indicate exact matching.
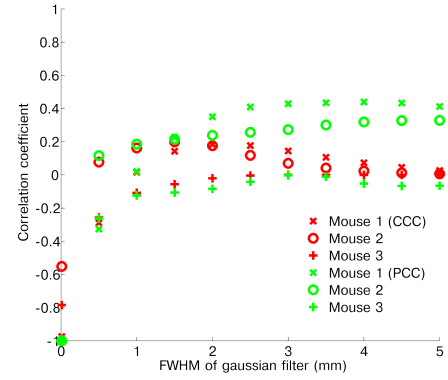
(b) Correlation of baseline and blurred data: comparison with inverted blurred data. A coefficient of -1 would indicate exact matching.

Figure C.2: Correlation of baseline and blurred data at different FWHM.

(a) Cooccurence matrix calculated by comparing the baseline image with itself.
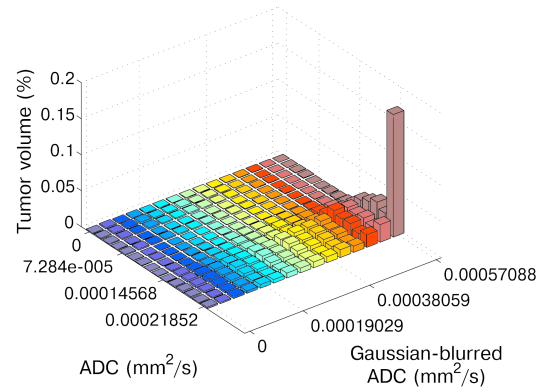
(b) Cooccurence matrix calculated by comparing the baseline image with the spatially variant blurred image.

Figure C.3: Cooccurence matrices were generated by binning from ADC values between 0 and the 75th percentile value within the tumor ROI. The PSF window used is 1.75 mm.

(a) Concordance correlation for different PSF windows with different binning conditions. Baseline images were compared to blurred baseline images.
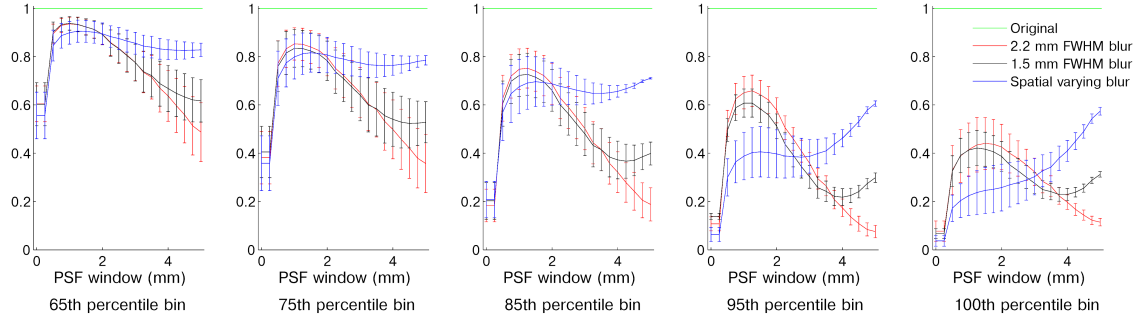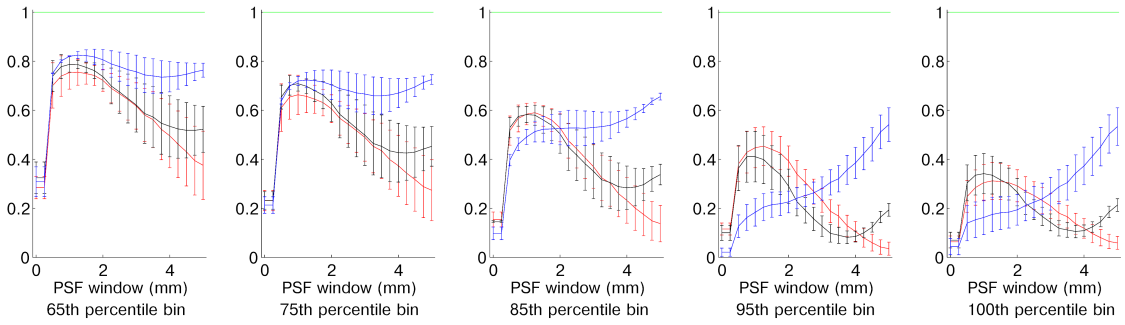

(b) Concordance correlation for different PSF windows with different binning conditions. Baseline images were compared to blurred inverted baseline images.

Figure C.4: Concordance correlation coefficients for cooccurence matrices compared to the control matrix. Matrices were calculated using different bin locations (percentile bin denotes the maximum histogram bin value) and PSF windows. Error bars denote standard error.

images. This makes sense, since Gaussian filters tend to cause spillover of high intensity voxels into low intensity regions and hence low intensity structures in the $Baseline_{inverted}$-blurred images are masked to a greater extent compared to the high intensity structures observed in the $Baseline_{original}$-blurred images.

Thirdly, the highest CCC was achieved in general for all binning conditions was observed with a PSF window ~1 mm. For images blurred with a spatially variant filter, a secondary high CCC peak was observed as the PSF window approached 5 mm. 1 mm is approximately half the FWHM of the Gaussian filters applied to the PET datasets. Thus, this should be the approximate radius which we expect a cooccurring voxel to lie compared to the voxel of interest. This relationship between structure resolvability and PSF window is supported by Valckx and Thijssen, who found that altering the PSF window as a function of speckle size in echographic images can affect the cooccurence matrix method's ability to resolve structures [293].

The trend towards high CCC for spatially variant filted images is due to the fact that the tumors being considered were ~5 mm. Thus, most of the tumor ROI voxels would cooccur with each other with a large PSF window.

Finally, we observed that the highest CCC are obtained using the 1 mm PSF window for maximal bin values at the 65th–85th percentile range. Maximal bin values above this resulted in reduced CCC values. The choice of optimal bin size and binning methods for cooccurence matix analysis is a subject of active investigation [294, 295, 296]. Both Handrick *et al.* [295] and Kim *et al.* [296] reported that nonlinear binning methods which adjust bin sizes depending on the histogram data were better than linear binning methods at tissue classification of CT images. This is reflected in our results, as linear binning (minimum value = 0, maximum value = maximum ADC value) showed the worst CCC with the baseline-baseline cooccurence matrix. The 65th–85th percentile binning performed better, possibly because higher intensity values are clustered into a smaller number of bins. The optimal binning method may be dependent on the question being asked. For example, in section 3.4 we wanted to correlate voxels with high ADC values with voxels with high ^{64}Cu-antibody uptake. Thus, a binning method that clustered high PET intensities above a threshold value into a subset of matrix bins that was used is suitable for this purpose. Further investigations are required to identify more generalized guidelines for choosing the optimal binning method for cooccurence

matrix generation.

C.3 Conclusion

We explored the effects of PSF window and binning method on cooccurence matrices generated between images with different spatial resolutions. The optimal PSF window is dependent on the spatial resolution of the imaging modality being considered. For PET-like images, we found the optimal PSF window to be approximately half the FWHM of the image. The choice of histogram bins can also affect cooccurence matrix results. Cooccurence matrices are being increasingly applied to PET and MRI images [297, 298, 299]. Further studies are needed to refine this method for the analysis of PET/MRI datasets.

Appendix D

Synchronous PET/MRI Software Code

D.1 MRI Code Implemented in Paravision Environment

D.1.1 PET_FLASH.ppg, a Modified Bruker FLASH Sequence to Include Syncing Modules

```
;************************************************************

;

; Copyright (c) 2001 - 2003

; Bruker BioSpin MRI GmbH

; D-76275 Ettlingen, Germany

;

; All Rights Reserved

;

; PET_FLASH - a gradient echo imaging method

;

; Set for Synchronised PET/MR

;

;************************************************************

;

; d0 - TR padding

; d1 - T1 padding
```

Modifications in italics.

```
; d2 - T2 padding

; d3 = PVM_RiseTime

; d4 = PVM_RampTime

; d8 = CONFIG_amplifier_enable

#include<Avance.incl>

#include <DBX.include>

preset off

define delay denab

define delay d4d10u

define delay d5d20u

define delay d0d40u

define delay d4d2

"denab = d3 - de + depa"

"d4d10u = d4 +10u"

"d5d20u = d5 +20u"

"d0d40u = d0 -40u"

"d4d2 = d4 + d2"

"l3 = l1 + ds"

#include <PrepModulesHead.mod>

#include <FlowSatinit.mod>

#include <MEDSPEC.include>

lgrad r2d<2d> = L[1]

zgrad r2d

lgrad r3d<3d> = L[2]

zgrad r3d

#include <PET_MR_SYNC_A.mod>

;MR sequence started and trigger sent to the PET system,

;we now initiate pre-pulse sequence setup

lo to decr times DS
```

```
lgrad slice = NSLICES

zslice

10u recph ph1
```

; *By now, the PET module should be ready. We then start the MR sequence and*

; *tell the PET system to start acquisition simultaneously.*

#include <PET_MR_SYNC_B.mod>

```
start, 10u

if(PVM_BlBloodOnOff)

{

#include <TriggerPerPhaseStep.mod>

}

#include <blblood.mod>

#include <TriggerPerPhaseStep.mod>

#include <SelSliceIr.mod>

#include <tagging.mod>

;—————————————-start of the main loop ————-

slice, 10u fq8b:f1

#include <TriggerPerSlice.mod>

;—————————————-preparation modules ————-

#include <FlowSat.mod>

subr SatSlices()

#include <MagTrans.mod>

#include <FatSup.mod>

d6 grad{(0)|(0)|(t9)}

;—————————————-slice selection——————

d3 grad{(0)|(0)|(t0)} fq1:f1

d8 gatepulse 1

p0:sp0 ph0

d4d10u groff
```

```
if(PVM_ppgFlag1) ;long TE mode
{
;————————————————-slice rephase————————
d10 grad{(0)|(0)|(t1)}
d4d2 groff
;————————————————-read dephase + phase encoding—-
d11 grad{(t2)|r2d(t3)|r3d(t4)}
d4d10u groff
}
if(!PVM_ppgFlag1) ;short TE mode
{
;————————-slice rephase, read dephase, phase encoding—-
d10 grad{(t2)|r2d(t3)|(t1)+r3d(t4)}
d4d2 groff
}
;————————————————-frequency encoding—————
denab REC_ENABLE grad{(t5)|(0)|(0)}
ADC_INIT_B(NOPH, ph2) ;ph1 is used (see recph)
aqq ADC_START
;———————————————-read spoiler + phase encoding—-
d11 grad{(t6)|r2d(t7)|r3d(t8)} ; 2nd and 3rd dims
d12 grad{(t6)| (0) | (0) }
d3 groff
d0 ADC_END
;————————————————-slice and movie loop————————
#include <FlowSatinc.mod>
if(NI > 1)
{
2.5u islice
```

```
lo to slice times NI

}

d20

;——————————————-averaging loop——————————-

if(NA > 1)

{

2.5u ipp1 ipp2

2.5u recph ph1

lo to start times NA

2.5u rpp1 rpp2

}

;——————————————-2d loop———————————

igrad r2d

lo to start times l3

"l3=l1"

;——————————————-3d loop———————————

igrad r3d

lo to start times l2

2.5u

lo to start times NAE

2.5u

#include <Evolution.mod>

2.5u

lo to start times NR

SETUP_GOTO(start)

exit

ph0 = 0

ph1 = 0 2 1 3

ph2 = 0 2 3 1
```

D.1.2 PET_MR_SYNC_A.mod

;***

```
;

; Caltech/ UC Davis PET/MR

;

; (c) 2010

;

;

; PET_MR_SYNC_A.mod - PET/MR Synchronous start module

;

;

;*****************************************************************

; Need to link to the methods

;Initialise

TTL4_HIGH

;

;Wait for the start signal from the PET program to begin

trignl4

TTL4_HIGH
```

D.1.3 PET_MR_SYNC_B.mod

;***

```
;

; Caltech/ UC Davis PET/MR

;

; (c) 2010

;

;

; PET_MR_SYNC_B.mod - PET/MR Synchronous start module
```

```
;

;

;*******************************************************

; Need to link to the methods

; Now Other prep stuff done, we start the sequence

TTL4_LOW

trigne4

TTL4_HIGH
```

Appendix E

MATLAB Implementation of an Unique Identifier for Multimodal Data Linkage

%% Make a Multimodal imaging header extension

% Define ecode = 30 Need to register with NIFTI

clear all

% Multimodal ID self first

ecodeA = 30;

% Modalities

%{

PET : standard positron emission tomography dataset

MRI : standard magnetic resonance imaging dataset

DCEMRI: dynamic contrase enhanced MRI dataset

DCEPET: dynamic contrast enhanced PET dataset

DWI :

CFM : Confocal microscopy

unique identifier is the same for all the datasets that belong together.

%}

uid = datestr(now, 30);

ext.section(1).ecode = ecodeA;

MODAL = unicode2native(fullfile('PET', 'MRI', uid)); % This would encode a PET image data which has an associated standard MRI dataset linked to it.

ext.section(1).edata = MODAL;

verify_nii_ext(ext)

% To store this extension.

%nii.ext